

Air Force Institute of Technology

AFIT Scholar

Theses and Dissertations

Student Graduate Works

3-2006

The Simulation of Off-axis Laser Propagation Using HELEEOS

Scott L. Belton

Follow this and additional works at: <https://scholar.afit.edu/etd>



Part of the [Plasma and Beam Physics Commons](#)

Recommended Citation

Belton, Scott L., "The Simulation of Off-axis Laser Propagation Using HELEEOS" (2006). *Theses and Dissertations*. 3286.

<https://scholar.afit.edu/etd/3286>

This Thesis is brought to you for free and open access by the Student Graduate Works at AFIT Scholar. It has been accepted for inclusion in Theses and Dissertations by an authorized administrator of AFIT Scholar. For more information, please contact richard.mansfield@afit.edu.



THE SIMULATION OF OFF-AXIS LASER PROPAGATION USING HELEEOS

THESIS

Scott L. Belton, Second Lieutenant, USAF

AFIT/GSS/ENP/06-01

**DEPARTMENT OF THE AIR FORCE
AIR UNIVERSITY**

AIR FORCE INSTITUTE OF TECHNOLOGY

Wright-Patterson Air Force Base, Ohio

APPROVED FOR PUBLIC RELEASE; DISTRIBUTION UNLIMITED

The views expressed in this thesis are those of the author and do not reflect the official policy or position of the United States Air Force, Department of Defense, or the United States Government

AFIT/GSS/ENP/06-01

THE SIMULATION OF OFF AXIS LASER PROPAGATION USING HELEEOS

THESIS

Presented to the Faculty

Department of Engineering Physics

Graduate School of Engineering and Management

Air Force Institute of Technology

Air University

Air Education and Training Command

In Partial Fulfillment of the Requirements for the

Degree of Master of Science (Space Systems)

Scott L. Belton, BS

Second Lieutenant, USAF

March 2006

APPROVED FOR PUBLIC RELEASE; DISTRIBUTION UNLIMITED

AFIT/GSS/ENP/06-01

THE SIMULATION OF OFF AXIS LASER PROPAGATION USING HELEEOS

Scott L. Belton, BS
Second Lieutenant, USAF

Approved:



Steven Fiorino (Chairman)

15 MAR 06
date



Richard Bartell (Member)

15 MAR 06
date



Richard Cobb (Member)

15 MAR 06
date

Abstract

Emerging technology high energy laser (HEL) weapon systems create a myriad of new threats to safety as well as security. One of the primary causes of these concerns is off-axis laser propagation caused by ever-present particulate and molecular scattering media in the atmosphere. The scatter from these aerosols and molecules can redirect some of the HEL's concentrated energy towards unintended targets such as the eyes of pilots, friendly fighters on the surface, or innocent bystanders. Of particular interest to the laser intelligence (LASINT) community is the possibility that off-axis irradiance from HEL weapon systems could be covertly measured with enough accuracy to provide critical information about HEL weight-power relationships, beam characteristics, and target intelligence information. The purpose of this research is to quantify how much off-axis propagation may occur in specific directions given a set of simulated HEL engagement scenarios involving different HEL characteristics, geometries, and atmospheric conditions. Further simulations assess the amount of information that can be derived about HEL platform characteristics and intended target from remotely measured off-axis intensity via inversion techniques. The High Energy Laser End-to End Operational Simulation (HELEEOS) software package is used to exploit its fast-running scaling law propagation methods and its robust probabilistic atmospheric database.

Acknowledgments

I would like to thank my mother and father for guiding me in the right direction and teaching me invaluable lessons that I will keep with me for the rest of my life. It was through their inspiration that provided me with the proper consistency and perseverance that enabled me to complete this research endeavor. I would like to express my sincere appreciation to Lt Col Steven Fiorino, for his guidance and support throughout the course of this thesis effort. He was enduring and tolerant with me from beginning to end. I would also like to show gratitude towards Dr. Rick Bartell and Matthew Krizo for the time spent and assistance with HELEEOS and Matlab coding. I would like to thank my friend in Texas for putting up with my one-sided talks about all of the tribulations I encountered. Also, for helping with grammar and spelling corrections and being so understanding. The insight was certainly appreciated. The most support that I received came from the faith that I have in God. I was able to stay focused, dedicated and complete this work without deviation.

Scott L. Belton

Table of Contents

	Page
Abstract.....	v
Acknowledgments.....	v
List of Figures.....	viii
List of Tables.....	x
List of Equations.....	xii
I. Introduction.....	1
Background.....	1
Problem Statement.....	1
Research Objective.....	2
Hypothesis.....	2
Research Focus.....	2
Summary of Current Knowledge.....	3
Approach/Methodology.....	3
II. Literature Review.....	5
Chapter Overview.....	5
Literature Review.....	5
History.....	5
Relevant Research.....	6
Atmosphere.....	8
Absorption.....	9
Thermal blooming.....	10
Scattering.....	11
Optical Turbulence.....	13
HELEEOS.....	13
III. Methodology.....	15
Chapter Overview.....	15
Definitions and Equations.....	15
Ocular Hazard.....	23
Summary.....	26
IV. Analysis and Results.....	28
Chapter Overview.....	28
Results of Simulation Scenarios.....	28

Scattering Phase Function	32
Intensity and Irradiance	36
Scenario 1.....	36
Scenario 2.....	38
Scenario 3.....	42
Scenario 4.....	44
Clouds.....	48
Clouds vs. Fog.....	50
Fog vs. Rain.....	51
Rain.....	52
Ocular Hazard Calculation	54
Relative Humidity	55
Time of Day.....	56
Laser Pointer Test.....	56
V. Conclusions and Recommendation.....	59
Conclusions of Research	59
Significance of Research.....	60
Recommendations for Action.....	60
Recommendations for Future Research.....	61
Appendix A.....	63
Appendix B.....	79
Bibliography	83
VITA.....	85

List of Figures

Figures	Page
1. Absorption of gases.....	10
2. Tangent Angles.....	20
3. Eye Sensitivity (WP_eyecolorsensitivity, 2004)	24
4. Absorption, scattering, and extinction of a desert atmosphere with desert aerosols	31
5. Scattering phase function of a desert atmosphere with desert aerosols	32
6. Scattering phase function conducted at Wright-Patterson Air Force Base, Caracas, Thule Air Base, and Kuwait.....	34
7. Scenario #1 Plane shooting laser straight down	37
8. Scenario #2 Plane shooting laser straight down	39
9. Relative Humidity.....	42
10. Scenario #3 Plane shooting laser horizontally	43
11. Scenario #4 Plane shooting laser horizontally-close	45
12. Intensity chart.....	46
13. Scattering phase function for cumulus clouds at 1.31525 micrometers	49
14. Scattering phase function for rain.....	52
15. Stratus Continental Clouds	64
16. Cumulus Continental Clean Clouds.....	65
17. Fog (1).....	66
18. Fog (2).....	67

Figures	Page
19. Very Light Rain	68
20. Light Rain	69
21. Moderate Rain.....	70
22. Heavy Rain.....	71
23. Extreme Rain	72
24. Relative Humidity 1st Percentile	73
25. Relative Humidity 50th Percentile.....	74
26. Relative Humidity 99th Percentile.....	75
27. Time of Day 0000-0300.....	76
28. Time of Day 0600-0900.....	77
29. Time of Day 1200-1500.....	78

List of Tables

Tables	Page
1. Summary of specific biological effects on the eye (Mallow, 1978).....	26
2. Atmospheric parameters table of a desert atmosphere with desert aerosols.....	29
3. Aerosol sizes and amounts for Wright-Patterson Air Force Base, Caracas, Thule Air Base, and Kuwait.....	35
4. Reference table for Figure 12	47
5. MPEs for ten seconds.....	55
6. Laser pointer simulation	57
7. Geometric Reference Table	63
8. Atmospheric Reference Table.....	63
9. Stratus Continental Clouds	64
10. Cumulus Continental Clean Clouds.....	65
11. Fog (1).....	66
12. Fog (2).....	67
13. Very Light Rain	68
14. Light Rain	69
15. Moderate Rain.....	70
16. Heavy Rain.....	71
17. Extreme Rain	72
18. Relative Humidity 1st Percentile	73
19. Relative Humidity 50th Percentile.....	74

Tables	Page
20. Relative Humidity 99th Percentile.....	75
21. Time of Day 0000-0300.....	76
22. Time of Day 0600-0900.....	77
23. Time of Day 1200-1500.....	78
24. Maximum Permissible Exposure (MPE) for small source ocular exposure to a laser beam (ANSI Z136.1, 2000).....	79
25. Maximum Permissible Exposure (MPE) for extended-source ocular exposure to a laser beam for long exposure durations (ANSI Z136.1, 2000).....	80
26. Maximum Permissible Exposure (MPE) for skin exposure to a laser beam (ANSI Z136.1, 2000).....	81
27. Parameters and Correction Factors (ANSI Z136.1, 2000).....	82

List of Equations

Equations	Page
1. Size Parameter	12
2. Scattering phase function in HELEEOS	12
3. Asymmetry parameter.....	16
4. Intensity scattering as a function of amplitude scattering.....	16
5. Phase function with amplitude function	17
6. Intensity as a function of scattering phase function.....	17
7. Scattering cross-section	18
8. Scattered intensity from a volume	18
9. Scattered intensity from 100 beam volume segments (no off-axis extinction)	18
10. Phase angle less than 90 degrees	19
11. Phase angle greater than 90 degrees	19
12. Pythagorean theorem	21
13. Cylindrical Volume.....	21
14. Diffraction- limited diameter	22
15. Scattered intensity from 100 beam volume segments (with off-axis extinction) .	23
16. Transmittance.....	23
17. Exitance.....	36

THE SIMULATION OF OFF AXIS LASER PROPAGATION USING HELEEOS

I. Introduction

Background

Today lasers have many different uses and can be found in much of today's new technology. They are used in DVD players, CD players, builder's leveling devices, precise cutting tools, guns (for aiming), communication devices, light shows, and in military applications. The word laser is an acronym for Light Amplification by the Stimulated Emission of Radiation. This research is primarily focused on High Energy Lasers (HELs), or weapon grade lasers being developed for the US Department of Defense (DoD).

Problem Statement

With the emerging HEL weapon systems, threats are posed to safety as well as security. One of the causes of these concerns is the off-axis laser propagation due to aerosols and molecules in the atmosphere. The atmosphere can scatter these HELs to unwanted places such as the eyes of pilots or to innocent bystanders. Additionally it is possible that the scattered HEL energy could be remotely detected and critical information about the origin, beam characteristics, and targets could be deduced. This thesis uses a high energy laser simulation model to determine how much off-axis propagation is occurring in specific directions as well as determine what information can be picked up about the platform and target of a HEL.

Research Objective

The High Energy Laser End-to-End Operational Simulation (HELEEOS) model is used in this thesis to analyze the off-axis propagation of a laser beam. By knowing the platform location and orientation of a laser beam, the intensity at an off-axis observing point or points is determined. Future work will consist of comparing HELEEOS with two similar software models from the National Air and Space Intelligence Center (NASIC) and applying what is learned from this research to the laser intelligence community.

Hypothesis

Given the three dimensional coordinates, the orientation, and the off-axis irradiance measurement of a HEL beam, along with local atmospheric conditions, the radiance of a platform and the irradiance of a target can be calculated using the Matlab based program, HELEEOS.

Research Focus

It is the goal of this research to develop a database spreadsheet of the off-axis propagation of high-energy lasers using HELEEOS as the vehicle. The initial part of this research entails becoming familiar with all of its limitations and capabilities of HELEEOS. Currently HELEEOS is still in its early stages with version one having been released earlier this year and version two still underway. Once all avenues of this off-axis laser propagation have been explored, future work will consist of comparing

HELEEOS with two other similar software programs that are currently in use by the National Air and Space Intelligence Center.

Summary of Current Knowledge

The HELEEOS model has been developed from an extensive review of literature on high-energy laser propagation from the past 25 years. HELEEOS is the first software program of its kind and it includes the integration of a variety of laser devices, beam control technologies, atmospheric compensation performance, and target interaction issues. The HELEEOS model assumes a continuous wave (CW) operation, that the beams are focused and uniform, fast steering mirrors (FSM) are available, and that the targets are flat plates (Bartell, 2004). This work represents the first attempt to use HELEEOS has never been used to study the off-axis HEL propagation of lasers.

Approach/Methodology

The primary purpose is to accomplish inverse analysis of off-axis laser propagation. A specific three-dimensional position is chosen that is not in the direct path of the laser simulated HEL beam. The amount of off-axis laser propagation that reaches this area in the simulation is used to determine the irradiance from the platform and the intensity reaching the target. It is assumed that all atmospheric conditions are known such as relative humidity, air pressure, temperature, cloud conditions, fog conditions, rain rate, wind speed, and visibility. Another assumption is that the orientation of the platform is known. If the distance between the target and the platform is known, the exact intensity reaching the target can be calculated. When the composition of the target

is known, HELEEOS then calculated a probability of kill. Furthermore, once the distance between the target and the platform is known, tables of distance versus irradiance on target are formulated. As the altitude decreases, particles and molecules increase, also increasing the extinction (absorption and scattering) of a beam. Note that scenarios with platforms and targets at the same altitude must be analyzed along with platforms and targets with different altitudes, affecting the study of beams over long distances where the platform and target are both at the same high altitude.

In addition, other variables still must be taken into account such as the wavelength of different lasers, thermal blooming, diffraction, optical turbulence, mechanical jitter (vibration from the aircrafts engine), and wave-front error. Real world calculations are simulated in HELEEOS with the assistance of Extreme and Percentile Environmental Reference Tables (ExPERT) and Directed Energy Environmental Simulation Tool (DEEST). ExPERT is a computer program that provides a probabilistic climate database for 299 sites around the world. For each of these land sites, ExPERT allows the user to view monthly and hourly percentile data, duration data, and yearly minimum and maximum values for altimeter setting, dew point temperature, absolute humidity, relative humidity, specific humidity, temperature, wind speed, and wind speed with gusts (Fiorino, 2004). DEEST is an optical turbulence decision aid used to simulate directed energy weapon scenarios. DEEST uses the Air Force Weather Agency (AFWA) MM5 forecast data. DEEST represents atmospheric optical turbulence values (Fiorino, 2004).

II. Literature Review

Chapter Overview

The intent of this chapter is to familiarize the reader with terms being used throughout the document, as well as to provide a review of some of the fundamental concepts and ideas. The low Earth atmosphere will be described along with some of its parameters and conditions; their relation to this work will be covered later. Some prior knowledge of atmospheric and laser physics is assumed.

Literature Review

The following section covers major concepts applying to HELEEOS and the off-axis propagation of a HEL. The usage of HELEEOS to calculate the off-axis propagation of a HEL has never been explored. In fact, little work has been done previously towards this exact topic. Literature of major concepts will clarify underlying issues. The relative research begins with a background of specific applications of HEL's followed by a description of the atmosphere. Next, a brief overview of absorption, thermal blooming, optical turbulence, and scattering is discussed. Subsequently, the software program HELEEOS is described in detail, and finally, a description of real world applications such as the Airborne Laser (ABL) program is covered.

History

In 1917, Albert Einstein was the first person to theorize about "Stimulated Emission." In 1954, Charles Townes and Arthur Schawlow invented the maser

(Microwave Amplification by Stimulated Emission of Radiation), which did not involve visible light. In 1958, Charles Townes and Arthur Schawlow theorized about a visible laser, an invention that would use infrared and/or visible spectrum light. Theodore Maiman invented the first ruby laser. Many people say that Theodore Maiman invented the first optical laser; some agree that Gordon Gould was the first. Gordon Gould was the first person to use the word "laser." There is good reason to believe that Gordon Gould made the first light laser. Gould was a doctoral student at Columbia University under Charles Townes, the inventor of the maser. Gordon Gould was inspired to build his optical laser starting in 1958, but he failed to file for a patent for his invention until 1959. As a result, Gordon Gould's patent was refused and others exploited his technology. Not until 1977 did Gould finally win his patent war and receive his first patent for the laser (About Inventors, 2005).

Relevant Research

The main focus of current research is on weapon grade HELs. In 1994, the DoD adopted Advanced Concept Technology Demonstrations (ACTD) to decrease the amount of time required for new technologies to transition from the developers' hands to the users' hands. The ACTD emphasizes technology assessment and integration rather than technology development only (Introduction, 2002). In 2001, an ACTD was proposed and funded for the Advanced Tactical Laser (ATL). The ATL, when operational, is expected to focus on military or law enforcement operations in urban or suburban environments. The ATL's HEL is projected to deliver a non-lethal or lethal force up to 15 kilometers away (Descriptions, 2002). Now underway at Boeing, with the assistance of Air Force

Research Laboratory (AFRL), the ATL is expected to be fully operational in the near future. Some speculated that it may be ready as soon as 2010 (*Popular Science*, 2005), but this is only a rough estimate. Some think that the ATL will be able to generate 100 to 300 kilowatts of optical power (Global Security, 2005) with a range of 20 kilometers and a diameter of up to 4 feet (*Popular Science*, 2005), but currently this is only a future vision.

The Missile Defense Agency (MDA) is developing a Ballistic Missile Defense System (BMDS) with the goal to “provide multiple engagement opportunities along the entire flight path of a ballistic missile” (MDA Link, 2005). The Airborne Laser (ABL) is one of the MDA’s highest priority programs. The mission of the MDA is to “Develop and field an integrated BMDS capable of providing a layered defense for the homeland, deployed forces, friends, and allies against ballistic missiles of all ranges in all phases of flight” (MDA Link, 2005). With this mission in mind, the MDA has been working diligently on the ABL. The ABL, also known as the YAL-1A, is a high-energy laser weapon system designed to destroy ballistic missiles. It is carried on a modified Boeing 747-400F freighter aircraft. AFRL, Team ABL, Boeing, Northrop Grumman, and Lockheed Martin are developing the ABL (Air Force Technology, 2005). The ABL consists of three lasers: the Chemical Oxygen Iodine Laser (COIL), the Track-Illuminating Laser (TILL), and the Beacon Illuminating Laser (BILL). The megawatt class COIL, which is the primary beam used for destroying the missiles, initiates in the back of the fuselage and goes all the way to the front, where it is aimed onto the target with a mirror. The low power TILL is used to determine the target's range and gives

initial information on the atmosphere. The illuminating laser tracks the target and provides aiming data for the primary beam. The kilowatt class BILL reflects light off the target to give data on the fast changing characteristics of the atmosphere along the path of the laser beam. The ABL is the first of its kind and is expected to be completed in 2006 (Air Force Technology, 2005).

Atmosphere

The atmosphere has many different effects on all lasers including HELs. The atmosphere of the Earth is divided into different layers. Those layers from highest to lowest are the thermosphere, mesosphere, stratosphere, and troposphere, respectively. This research concentrates on the stratosphere and the troposphere because 99% of the atmosphere's mass is contained in these two layers. Petty (2004) states that the atmosphere contains 78.1% Nitrogen (N_2), 20.9% Oxygen (O_2), and the other 1% is made up of Argon (Ar), Carbon Dioxide (CO_2), Methane (CH_4), Nitrous Oxide (N_2O), Carbon Monoxide (CO), Ozone (O_3), and other trace gasses (Petty, 2004:170). Water vapor (H_2O) varies greatly (0-2%) depending on time of day, altitude, and location (Petty: pg 2004). Some of these gasses affect laser beams and others do not. Air pressure decreases as the altitude increases; for that reason, there are more gas molecules in the low Earth atmosphere. The logarithmic decrease of air pressure and density with altitude is a condition that results in laser beams being more affected closer to the ground.

Absorption

The electromagnetic spectrum includes wavelengths that range from 0.01 microns to more than one millimeter (Petty, 2004: pg 55). The wavelengths that are covered in this research are: 0.4 microns, 0.55 microns, 0.68 microns, 1.0623 microns, 1.31525 microns, 1.624 microns, 3.8 microns, and 10.6 microns (Bartell, 2004: sect 2.3; Petty, 2004: pg 55). Figure 1 illustrates the amount of absorption that takes place from the different gases in the atmosphere. Notice that the gases have different transmissions depending on the wavelength of electromagnetic beam. Absorption occurs when a particle of light goes into a medium and is not transmitted or reflected. This usually causes the medium, whether it is an atom or molecule, to increase in temperature. Absorption decreases peak intensity and helps to induce thermal blooming in HEL beams (LSW Short Course, 2005:sect. 6).

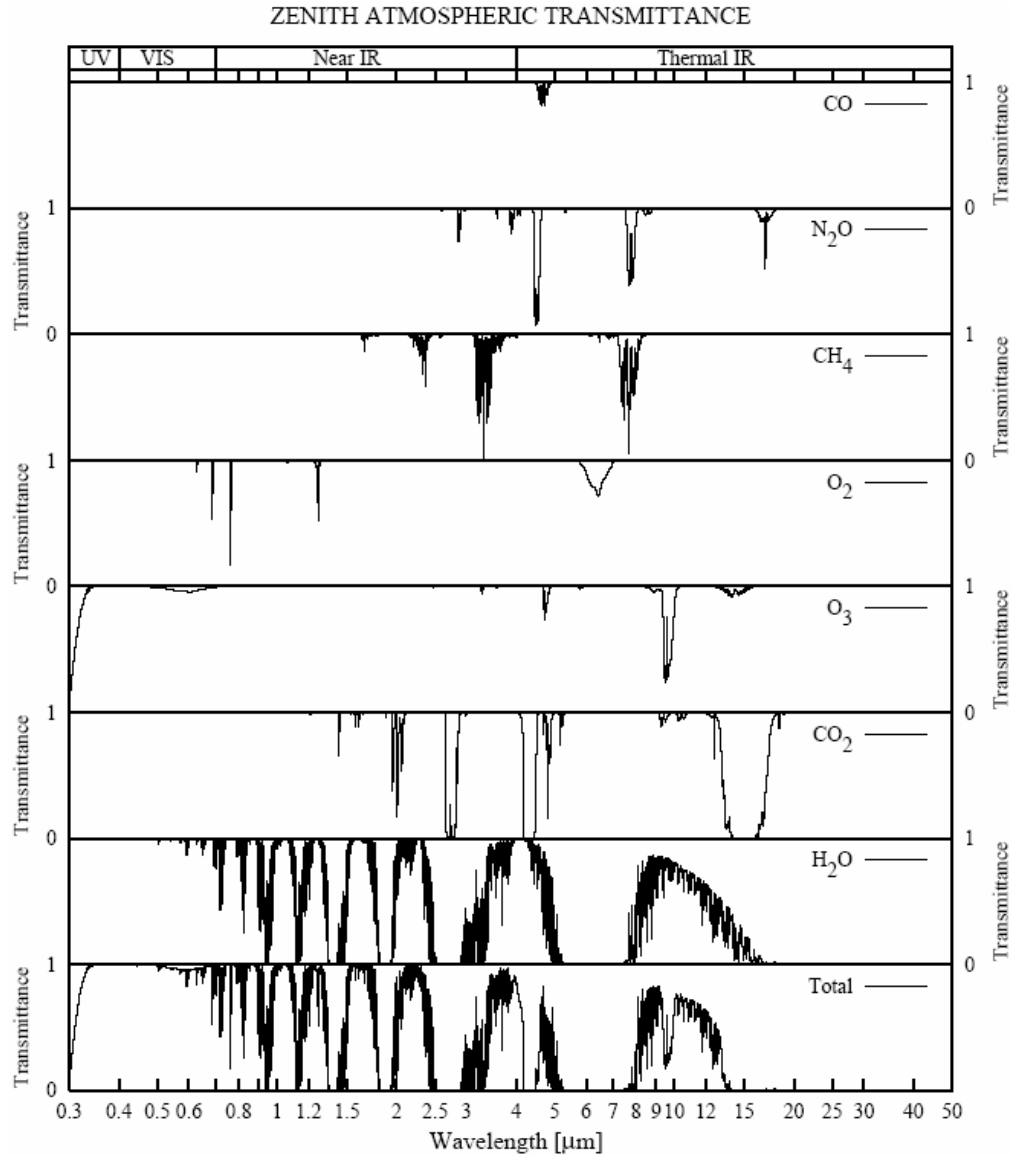


Figure 1: Absorption of gases

Thermal blooming

According to the Photonics Directory, thermal blooming is the effect that characterizes an intense laser beam that is passed through an absorbing medium, causing the absorbed energy to produce density changes in the absorbing medium that can alter the intensity distribution of the beam and shift it away from the intended direction of

propagation (Photonics, 2005). In short, thermal blooming is caused by laser heating of the atmosphere (LSW Short Course, 2005:sect. 6, pg 46).

Thermal blooming, in general, is negligible and can be ignored in very high altitudes (above 11,000 meters) due to low absorption. The ABL is expected to operate primarily at such altitudes. Thermal blooming can also be ignored where there is minimal atmosphere, with the Space-Based Laser (SBL) engagement scenarios. Furthermore, thermal blooming can be ignored where HEL's operate away from absorption lines and aerosols. Thermal blooming is important for low altitudes with high absorption such as with tactical HEL engagements, and anticipated ATL operations. (LSW Short Course, 2005:sect. 6, pg 44)

Scattering

Extinction of the HEL beam is caused by both absorption and scattering, but scattering will be the main focus of this research. Scattering occurs when a particle of light hits a medium and changes direction. Molecular and aerosol scattering remove intensity from the beam. There are primarily two types of scattering that can take place, Rayleigh scattering and Mie scattering. Rayleigh scattering occurs when the wavelength of the beam is smaller than the radius of the particle and Mie scattering occurs when the wavelength of the beam is just about equal to or larger than the radius of the particle (LSW Short Course, 2005:sect. 6). Mie scattering takes place when the size parameter is between 0.2 and 200, while Rayleigh scattering takes place when the size parameter is between 0.002 and 0.2. The size parameter is defined as

Equation 1: Size Parameter

$$\chi \equiv \frac{2\pi r}{\lambda}$$

where r is the radius of the particle and λ is the wavelength of the beam. As the size parameter increases the amount of forward scattering increases as well. This occurs whether the particle has spherical shape or not.

The scattering phase function angle will be the major factor. The equation in HELEEOS that calculates this value is as follows,

Equation 2: Scattering phase function in HELEEOS

$$\frac{P(\theta)}{4\pi} = \frac{\lambda^2}{4\pi^2} \sum_{i=r_{\min}}^{r_{\max}} n(r) \frac{i_1 + i_2}{2} \Delta r_i$$

where λ is the wavelength of the beam, $n(r)$ is the particle size distribution, $i_1 = S_1 S_1'$, $i_2 = S_2 S_2'$, and S_1 and S_2 are dimensionless intensity or amplitude functions. This determines the angle at which photons are scattered in. The scattering phase function is used to calculate how much laser energy is scattered in any off-axis direction. Here, the single scatter of a photon is being calculated. The only way that a particle will be scattered once is if the medium that it is traveling through is very thin or if the single scatter albedo is closer to zero. This would give the photon a chance to be absorbed before it is scattered a second time. Multiple scattering is when a photon is scattered more than once and calculating this is much more difficult. Photons can be scattered

hundreds of times in all directions, causing some photons to scatter back into the original axis of the laser beam. The current research does not take into account multiple scattering because the atmosphere being studied has an asymmetry parameter close to one. Adding scattering and absorption together gives a total, which is called extinction. Extinction is the amount of a laser beam energy that does not reach its intended target along the original axis. Transmission is the amount of a laser beam reaching its intended destination along the original axis. Extinction is not the only degrades effect of the atmosphere on HEL beams – optical turbulence is an example of another.

Optical Turbulence

Optical turbulence causes distortion of a laser beam; it is similar to irregular or random motions in a fluid. Some sources of this turbulence are convection from hot surfaces, wind shear, weather systems, and laser heating (thermal blooming). Optical turbulence also causes variations in air temperature and composition as well as changes in index of refraction (LSW Short Course, 2005:sect. 6, pg 21). As altitude increases, optical turbulence decreases. Therefore at extremely high altitudes (above the stratosphere) it becomes negligible.

HELEEOS

The High Energy Laser End-to-End Operational Simulation (HELEEOS) is a Matlab based software program that simulates lasers from platform to target. AFIT's Center for Directed Energy developed HELEEOS. HELEEOS incorporates all atmospheric degradation effects, including previously covered thermal blooming,

molecular and aerosol absorption, scattering extinction, and optical turbulence. Atmospheric parameters that are covered include profiles of temperature, pressure, water vapor content, and optical turbulence. HELEEOS can simulate static as well as dynamic engagements (Bartell, 2004). HELEEOS has the ability to simulate lasers with many different wavelengths ranging from 0.355 microns to 10.6 microns. HELEEOS also uses Extreme and Percentile Environmental Reference Tables (ExPERT) and Directed Energy Environmental Simulation Tool (DEEST) to aid in realistic atmospheric laser simulation. ExPERT is a database with different atmospheric characteristics for eight different land regions overlaid by five upper air regions, all with nine water vapor percentile cases for summer and winter. DEEST allows use of C_n^2 vertical profiles predicted from numerical weather forecasting data (MM5 or WRF). HELEEOS also allows the probability of kill to be estimated. The probability of kill is not necessarily just destroying a target. It depends on the initial goal of the laser beam being radiated.

Irradiance (exitance at laser aperture) of the laser has the units of $W m^{-2}$ and intensity at the off-axis point has the units of $W m^{-2}Sr^{-1}$. Irradiance in this research is defined as the time averaged radiant flux density in all directions. Intensity is when the flow of energy (light) is nonparallel and when the detector collects the energy confined to a range of directions specified by a small element of solid angle.

The above information covers previous work that has been performed allowing a good starting point for this research. Scattering is the focal point of this thesis, but other atmospheric effects are included to fully accomplish the goals of this research.

III. Methodology

Chapter Overview

The study of off-axis HEL scattering is currently a very important concept. Total extinction consists of absorption and scattering. Absorption is important but not as important as scattering in this case absorption's attenuating effects are mainly confined to the HEL beam. On the other hand, as intensity is increased the amount of energy scattered off-axis is increased. This research considers two specific scenarios with respect to off-axis scattering. The first is the safety of the pilots who are flying any aircraft that propagates a HEL. Extended and repeated exposures to these beams can be harmful for the eyes as well as the skin. The second scenario is a HEL aircraft on a sensitive mission which needs to covertly strike a target. For instance, say there is a target in a populated area. Friendly forces may desire this target be hit, but may not want the surrounding population affected – an ideal scenario for an airborne HEL, if such a weapon is available. Off-axis scattering from the HEL beam may give the unfriendlies enough insight to realize what is taking place, assuming they have receivers set up to sense this scattered energy.

Definitions and Equations

The direction of any laser beam that is being analyzed is a vector defined as $\hat{\Omega}$ and the direction of a specific photon coming off of that beam will be a vector defined as $\hat{\Omega}'$. The phase function will be defined as $p(\hat{\Omega}', \hat{\Omega})$ and since multiplying $\hat{\Omega}$ and

$\hat{\Omega}'$ is equal to $\cos \Theta$, the phase function will be referred to as $p(\cos \Theta)$, with Θ being the angle between $\hat{\Omega}$ and $\hat{\Omega}'$. The asymmetry parameter g is the average value of $\cos \Theta$ for a large number of scattered photons and it can be calculated by the following integral (Petty, 2004).

Equation 3: Asymmetry parameter

$$g \equiv \frac{1}{4\pi} \int_{4\pi} p(\cos \Theta) \cos \Theta d\omega$$

Values of g range from -1 to 1, with 1 being photons that are scattered straight forward as if they were not scattered at all, and -1 being photons that are scattered backwards the same way that they came. A value of zero means equal forward and backward scattering.

The major goal of this investigation is to measure the amount of scattered intensity that is reaching the off-axis observing point. Following Stephens (1994), the equation,

Equation 4: Intensity scattering as a function of amplitude scattering

$$I_{SCA} = \frac{|S(\Theta)|^2 I_o}{k^2 R^2}$$

relates amplitude function $S(\Theta)$ (described as a scattering pattern) and initial beam intensity I_o to scattered off-axis intensity. The next equation,

Equation 5: Phase function with amplitude function

$$\frac{1}{4\pi} P(\Theta) = \frac{|S(\Theta)|^2}{k^2 C_{SCA}}$$

relates the scattering phase function $P(\Theta)$ to amplitude function (Stephens, 1994).

Combining these two equations gives the equation,

Equation 6: Intensity as a function of scattering phase function

$$I_{SCA} = \frac{P(\Theta) C_{SCA} I_o}{4\pi R^2}$$

where C_{SCA} is the scattering cross section (dimensions of area) of the scattering particle, I_o is the initial incident intensity of the scattering particle, and R is the distance between the receiver and the beam. Typically scattering cross section has the units of m^2 , scattered intensity has the units of $Wm^{-2}Sr^{-1}$, R has the units of m , and the phase function is dimensionless. This equation allows the scattered intensity to be calculated from the phase angle, which is an output of the Wiscombe (1980) Mie scattering module within HELEEOS. Unfortunately, Equation 6 only yields the scattered intensity due to one particle at the off-axis point. Therefore the scattering particle number density N (per unit volume) is needed to account for the scattered intensity due to a distribution of particles. Since the scattering cross section is equal to the volume scattering coefficient divided by the number density, multiplying by the number density N would cause the number densities on top and bottom to cancel out leaving just the volume scattering

coefficient β_{SCA} (units of inverse length). The scattering cross-section is related to β_{SCA} via:

Equation 7: Scattering cross-section

$$C_{SCA} = \frac{\beta_{SCA}}{N}$$

Combining Equations 6 and 7 yields the scattered intensity as a function of scattering angle and volume scattering coefficient

Equation 8: Scattered intensity from a volume

$$I_{SCA} = \frac{P(\Theta)\beta_{SCA}I_o}{4\pi R^2} dv$$

where dv is the scattering volume.

Currently, the way HELEEOS analyzes laser beams is by splitting the beam up into 1,000 different segments. This research analyzes laser beams by splitting the beam up into 100 different segments, to reduce the computational expense. The intensity being scattered onto the off-axis receiver of each one of these segments is calculated separately and then added to give the total scattered intensity. Ultimately, the equation of scattered intensity becomes,

Equation 9: Scattered intensity from 100 beam volume segments (no off-axis extinction)

$$I_{SCA} = \sum_{i=1}^{100} \frac{P(\Theta)_i \beta_{SCA_i} I_{O_i}}{4\pi R_i^2} dv_i$$

Each one of the segments being analyzed has a different phase angle $P(\Theta)_i$. A few calculations are necessary to compute these angles. Referring to Figure 2 below, the equation of Line B is found from the platform to the target using the equation of a line. Next, the distance from the point where the off-axis receiver is to line B is found (labeled as distance R). The equation of this line must also be found, which is represented as line A in the figure. Line A is orthogonal to Line B, so the dot product of these two lines is equal to zero. The point where Line A and Line B intersect is calculated and this is called point P1. The distance from point P1 to the platform is represented as D1 and the distance from point P1 to the target is represented as D2. The phase angle for each of the segments of the beam that are between point P1 and the platform is calculated using Equation 10.

Equation 10: Phase angle less than 90 degrees

$$\Theta = \arctan\left(\frac{R_p}{D1}\right)$$

The phase angle for each of the segments of the beam that are between point P1 and the target is calculated using Equation 11.

Equation 11: Phase angle greater than 90 degrees

$$\Theta = 180 - \arctan\left(\frac{R_p}{D2}\right)$$

Each segment has a different value for D1 or D2. D1 or D2 is calculated by adding the length of a specific number of segments together.

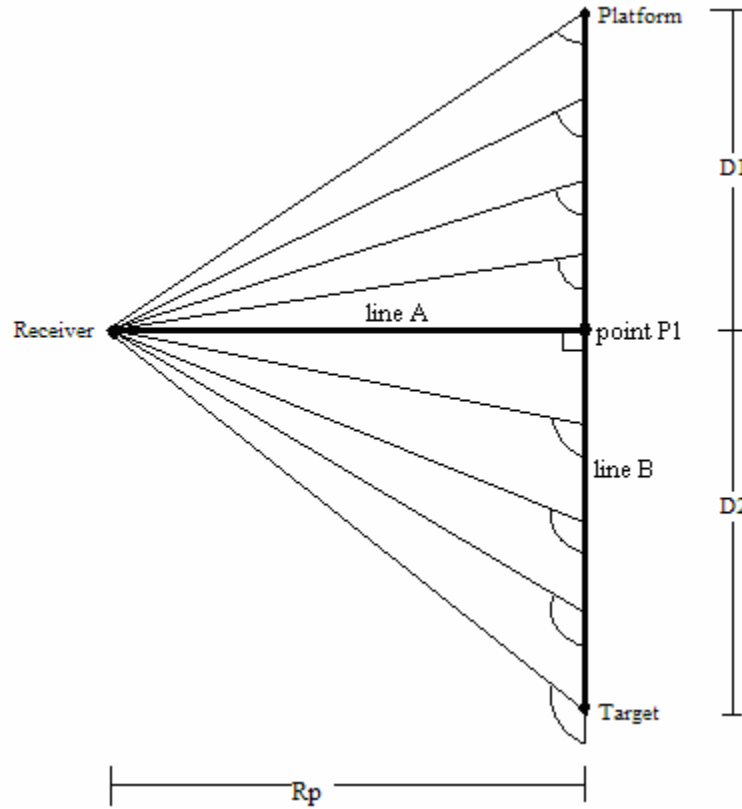


Figure 2: Tangent Angles

The phase function $P(\Theta)$ uses the phase angle Θ to determine a value. HELEEOS generates phase function values for every even phase angle from 0 to 180. If the phase function of a phase angle needs to be calculated that is between these two even phase angles linear interpolation is performed. The equation of a line connecting the two closest points will be calculated. For example, if the phase function of 43.23 degrees needs to be found, HELEEOS outputs the following information:

Phase Angle Θ	Phase Function $P(\Theta)$
42	0.059
44	0.053

The slope and end points of this line segment are plugged into the equation of a line. Next, the phase angle 43.2 degrees is plugged into this equation to find the corresponding phase function value.

The initial incident intensity I_{o1} for the first segment (closest to the laser aperture) is the intensity coming out of the laser (which is assumed to equal the exitance within the beam). The initial incident intensity I_{o2} for the second segment is the initial incident intensity of the laser minus the extinction from the first segment. The initial incident intensity I_{o3} for the third segment is the initial incident intensity of the laser minus the extinction from the first and second segment (etc....). The following equation,

Equation 12: Pythagorean theorem

$$R = \sqrt{x^2 + y^2 + z^2}$$

is used calculate the distance R_i , which is the distance of the off-axis receiver to each segment of the beam.

The value dv_i is the volume of the segment being considered and it is equal to the volume of the cylinder of the beam represented by that segment. The resultant equation, is

Equation 13: Cylindrical Volume

$$dv = \pi \left(\frac{d}{2} \right)^2 h$$

where d is the diameter of the beam and h is the length of that segment. When looking at the entire laser beam, the diameter of the beam changes. In other words, the beam has a specific diameter when it leaves the aperture and it focuses down to a very small diameter. The beam focuses down to a minimum size, which is called diffraction-limited diameter (D) and is calculated in HELEEOS by the following equation,

Equation 14: Diffraction- limited diameter

$$D = 2.44 \times \left(\frac{\text{Wavelength}}{\text{ApertureDiameter}} \times \text{SlantRange} \right)$$

where *SlantRange* is the distance traveled of the laser beam.

One last factor must be taken into consideration when calculating the scattered intensity at an off-axis point. Equation 9 does not include off-axis extinction. The final addition to this equation is the transmittance from each of the scattering beam segments to the off-axis observer. HELEEOS can be configured to calculate each of these off-axis transmittances. The way that HELEEOS computes any transmittance is by simulating a laser beam from a platform to a target and calculating the amount of irradiance reaching the target. The current control-script for this research uses HELEEOS to calculate the transmittance by simulating a laser beam from the segment being analyzed to the off-axis point. Each segment of the beam that is being analyzed is a different distance away from the observer and has a different transmittance value. This is because atmospheric transmittance decreases with altitude, and each segment can be at a different altitude. The scattered, off-axis intensity is then multiplied by the transmittance value that HELEEOS generates. The end equation is

Equation 15: Scattered intensity from 100 beam volume segments (with off-axis extinction)

$$I_{SCA} = \sum_{i=1}^{100} \frac{P(\Theta)_i \beta_{SCAi} I_{oi} t_i}{4\pi R_i^2} dv_i$$

where t is transmittance. The transmittance equation is,

Equation 16: Transmittance

$$t(s_1, s_2) \equiv e^{-\int_{s_1}^{s_2} \beta_{ext} dx} \approx e^{-\beta_{ext} \cdot R}$$

where S_1 is the beginning of the optical path and S_2 is the end of the optical path being calculated and β_{ext} considers both absorption and scattering of the scattered off-axis intensity.

Ocular Hazard

When determining the amount of irradiance entering the eye from a laser beam, a certain amount of information must be known about the eye. The diameter of the pupil must be known in order to find the area that the rays are passing through. Also, the field of view must be known to find the solid angle that a human eye can see. For one eye, the maximum field of view horizontally is approximately -59 degrees to 110 degrees, and vertically from -70 degrees 56 degrees (looking straight forward is zero degrees horizontally and vertically). These angles are limited by the nose (horizontally) and by the eyelids (vertically). The opposite eye has a maximum field of view that is the same,

but symmetrically reversed. Together the human eyes can see $\approx 4/3 \pi$ (4.1887) steradians, which is $1/3^{\text{rd}}$ of a total sphere. After 20-30 minutes of darkness the sensitivity of an eye can increase by as much as 250 times (6 magnitudes) due to a chemical effect that takes place in the retina of the eye. During the day the eye is most sensitive to green light, and at night there is a slight shift in this sensitivity to a shorter wavelength (closer to blue light). Below, Figure 3 displays the amount of sensitivity the eye has for different wavelengths of visible light during daylight hours.

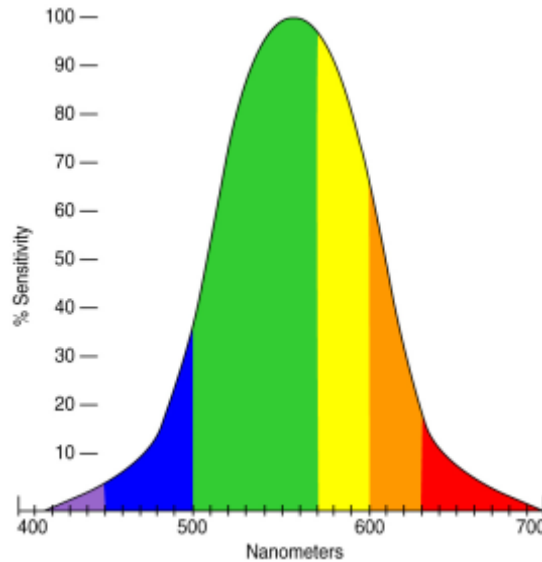


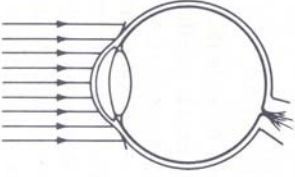

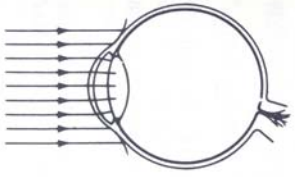
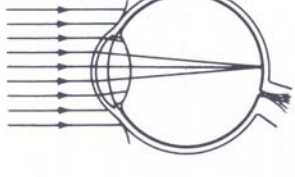
Figure 3: Eye Sensitivity (WP_eyecolorsensitivity, 2004)

The book “American National Standard for the Safe Use of Lasers” (ANSI Z136.1) is used as a reference to determine the amount of scattered intensity that is dangerous to the human eye. There is a value called the Maximum Permissible Exposure (MPE) that indicates if the amount of irradiance reaching the eye is potentially harmful. The International Commission on Non-Ionizing Radiation Protection (ICNIRP) sets the

MPE values. It is very important to know that the MPEs are not perfect. These values that distinguish “dangerous” and “safe” are derived from animal experiments and a limited number of human exposures. The tables that display these MPE values can be found in Appendix B. If any further referencing is desired please refer to ANSI Z136.1, 2000.

Table 1 below, shows how the human eye is affected by different wavelengths of electromagnetic energy. The table displays the effect of wavelengths ranging from Short Ultraviolet up to Far Infrared. The cornea, which is the outer layer of the eye, absorbs the wavelengths of .1 micrometers-0.315 micrometers and 1.4 micrometers-1,000 micrometers. The primary lens absorbs wavelengths of 0.315 micrometers-.400 micrometers, which underlies the cornea. The retina absorbs wavelengths of 0.4 micrometers-1.4 micrometers. The wavelengths of 0.4 micrometers-.7 micrometers correspond to visible light. This means that the portion ranging from .7 micrometers to 1.4 micrometers could be the most harmful since this is invisible (or only barely visible) and reaches the retina. Combining this with the dilation of the pupil at night, these wavelengths could be even more harmful. Note that wavelengths larger than 1.4 micrometers are equally as harmful for the skin as well as the eye according to the MPE charts in Appendix B. Reviewing Table 1 shows that the wavelengths less than 1.4 micrometers penetrate the eye down to the retina, whereas the retina absorbs the wavelengths greater than this.

Table 1: Summary of specific biological effects on the eye (Mallow, 1978)

Spectral Region	Absorption Area	Eye Schematic Representation	Specific Biological Effects	Comments
Far-Infrared (IR-B and IR-C) (1.4–1000 μm)	Cornea		<ul style="list-style-type: none"> • Minimal corneal lesion. • Loss of transparency of cornea or "glassworkers or furnaceman's" cataract. • Increased irradiance can cause more serious damage. 	A minimal corneal lesion is a small white area solely on the corneal epithelium, with the surface neither swollen nor elevated. ⁴ It appears within 10 minutes after exposure and heals within 48 hours without visible scars.
Short-Ultraviolet (UV-B and UV-C) (100–315 nm)	Cornea		<ul style="list-style-type: none"> • Excessive ultraviolet exposure can produce: <ul style="list-style-type: none"> – Redness – Tears – Secretion of mucus from the eyeball (conjunctival discharge) – Peeling or stripping off of the surface layer of cells from the cornea or connective tissue (stromal haze). • Damage to corneal epithelium by photochemical denaturation of proteins or other molecules (i.e., DNA, RNA, etc.). 	Damage to the corneal epithelium is probably of photochemical rather than thermal origin.
Near-Ultraviolet (UV-A) (315–400 nm)	Primarily Lens		<ul style="list-style-type: none"> • Lens can fluoresce. • Very high doses can cause corneal and lenticular opacities. 	
Light (400–700 nm) Near-Infrared (IR-A) (700–1,400 nm)	Retina and Choroid		<ul style="list-style-type: none"> • Mildest reaction may be simple reddening. • Minimal or threshold retinal lesion. • Increased retinal irradiance can cause large lesions, charring, hemorrhage, as well as gas formation, disruption of the retina and physical alteration of the eye structure. 	A minimal retinal lesion is the smallest visible change in the retina viewed with an ophthalmoscope. ⁴ It occurs within a full day after exposure and is a small white patch (likely coagulation).

Summary

This chapter outlined the equations used in this study to calculate the intensity of off-axis HEL beam scatter. These equations have been written in Matlab scripts and excel spreadsheets that feed HELEEOS. The excel spreadsheets allow the user to input wavelength, atmospheric conditions, and various geometries. Eventually these scripts

and spreadsheets will be incorporated into a Graphical User Interface (GUI) to run in conjunction with the current HELEEOS GUIs, and be released in a later version.

IV. Analysis and Results

Chapter Overview

This chapter examines in detail the results of the propagation simulation outlined in chapter 3. The outputs of these simulations include scattering and absorption comparisons, scattering phase function results, as well as different intensity values at different off-axis points in laser engagements. The values at the off-axis points are varied by varying the geometry altitude, the observer position with respect to the laser beam, as well as the atmosphere type. The cases of rain, clouds and fog are also analyzed. Obviously, every scenario or combination of atmospheres and laser wavelengths are not considered due to the time constraints of this thesis research project. The scenarios executed were strategically chosen with the thought of real laser engagements that are presently possible. Some of the chosen scenarios are extreme cases, which are included for testing purposes to better understand specific effects.

Results of Simulation Scenarios

As stated previously, when altitude increases, extinction decreases. Below in Table 2 is the atmospheric parameters table that illustrates this behavior by displaying multiple variables at different altitudes.

zero. Currently HELEEOS splits the laser beam up into 1,000 segments and outputs different values at each of these segment points. The table has been formatted to fit in the page so it is only displaying 16 of those 1,000 segments.

A review of Table 2 validates that extinction decreases as altitude increases. Looking even closer at scattering and absorption, it shows that neither value stays the same as altitude changes. This would mean that the best scenario for an adversary to pick up information from off-axis propagation would be a very low, horizontal laser engagement with a receiver above the laser at a higher altitude. The scenario would have the laser propagating through an atmosphere that has strong scattering patterns, and the scattered rays traveling toward the receiver would be experiencing a lower extinction giving the receiver a relatively high amount of unattenuated scattered intensity. Additionally the scenario in Table 2 shows that aerosols scatter more than absorb, and molecules absorb more than scatter. It should be noted that aerosols and molecule scatter energy differently based on scatterer size and wavelength. There are also different number densities for aerosols and molecules. The amount of scattering for aerosols in this case ($\lambda=1.315\mu\text{m}$) is orders of magnitude above the amount of scattering for molecules. In fact, the scattering from the molecules is so small in this case it could be ignored.

Figure 4 below is a graph of total (aerosol plus molecular) absorption, total scattering, and cumulative extinction for the Table 2 scenario.

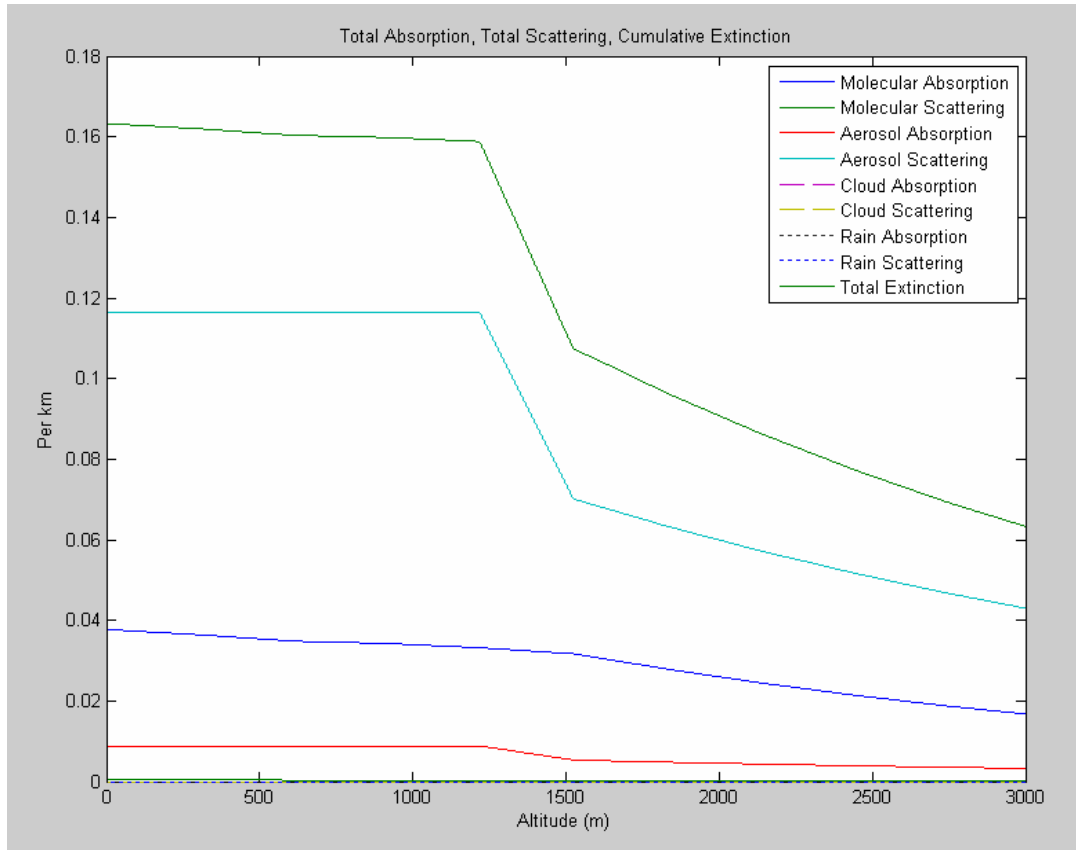


Figure 4: Absorption, scattering, and extinction of a desert atmosphere with desert aerosols

It is also a standard HELEEOS output plot. In Figure 4 the top line (green) is the total extinction, the second line (navy blue) is molecular absorption, the third line (teal) is aerosol scattering, the fourth line (red) is aerosol absorption, and the lowest line (light green) is molecular scattering. Since the total extinction is the sum of all of the other curves, it has the highest value. In this atmosphere, aerosol scattering is the strongest extinction factor followed by molecular absorption and aerosol absorption. The weakest extinction factor is molecular scattering, which is very close to zero.

Scattering Phase Function

The scattering phase function illustrates the direction that photons are scattered after coming in contact with aerosols or molecules. Figure 5 illustrates the scattering phase function vs. scattering phase angle for a 1.31525 micrometers laser in the desert scenario of Table 2.

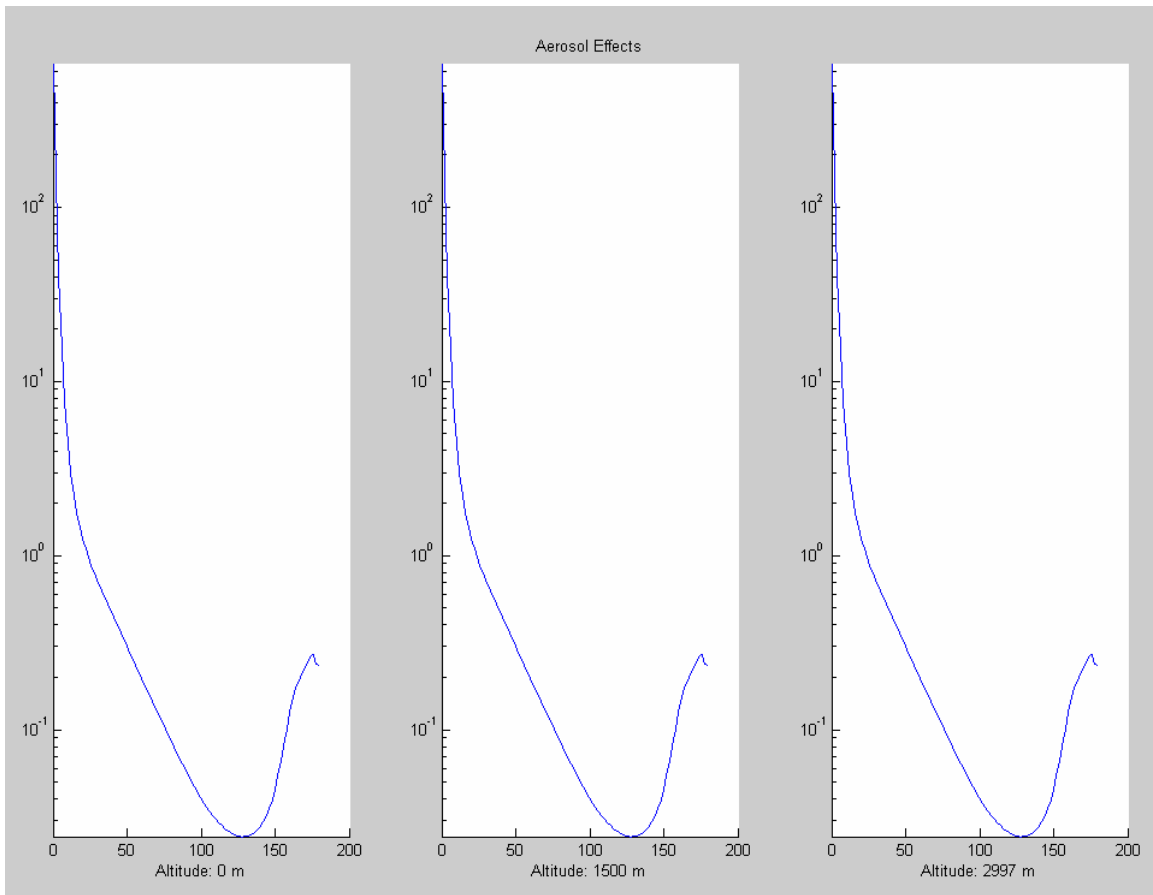


Figure 5: Scattering phase function of a desert atmosphere with desert aerosols

This is another example of a standard HELEEOS output plot. By default HELEEOS graphs the scattering phase function curves at the beginning of the beam, the midpoint,

and the end of the beam but can be changed to graph any three points along the beam. The vertical coordinate represents the scattering phase function value and the horizontal coordinate represents the phase angle. The phase angle is computed in radians but it is graphed in degrees. The scattering phase function as plotted has no units. The phase angle only goes up to 180 degrees because for Mie scattering it is symmetric in three dimensions. Phase function values vary greatly depending on the wavelength of the laser beam and the size distribution of the scatterers in the atmosphere in which the beam is propagating. Generally, the scattering phase function exhibits very strong forward scattering with some backscatter and relatively little side scatter.

There are four graphs below in Figure 6, which represent the different locations of Wright-Patterson Air Force Base, Caracas, Thule Air Base, and Kuwait, respectively. The individual site data used in Figure 6 are obtained from the ExPERT database in HELEEOS. They are all 50th percentile (average humidity), summer conditions. Each graph location displays wavelengths of 0.4 micrometers, 1.31525 micrometers, 3.8 micrometers, and 10.6 micrometers at an altitude of 3,000 meters. These graphs display strictly the scattering phase function, which is an illustration of the direction that photons are scattered after coming in contact with aerosols or molecules. Each graph behaves differently because there are different types of aerosols at these different locations. Caracas has the highest amount of side scattering, Kuwait has the smallest amount of side scattering, and the scattering patterns of Wright-Patterson AFB and Thule AB are very similar. Side scattering corresponds to the scattering at about 120 degrees, forward

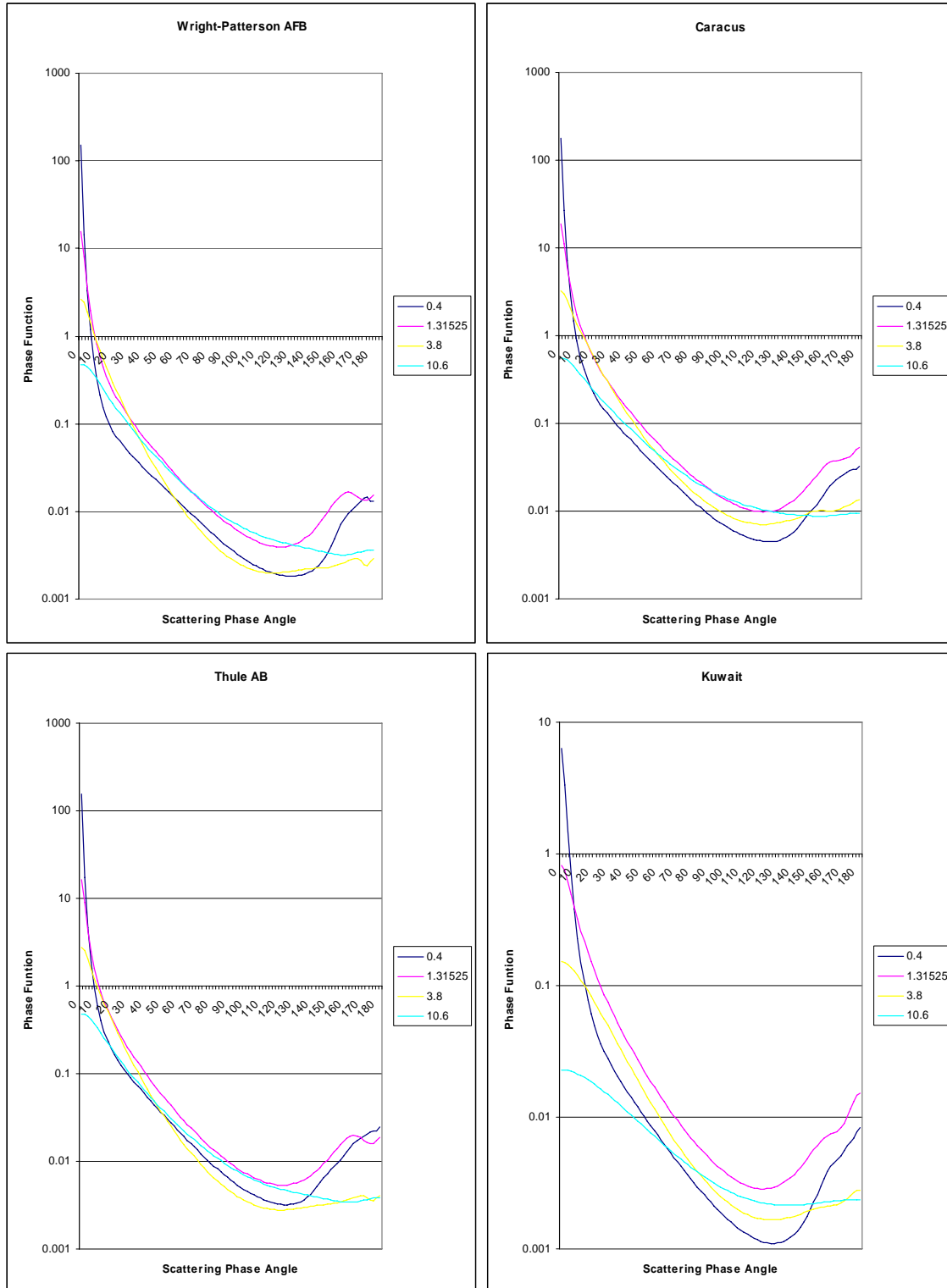


Figure 6: Scattering phase function conducted at Wright-Patterson Air Force Base, Caracas, Thule Air Base, and Kuwait

scattering corresponds to scattering less than 30 degrees, and backscattering corresponds to scattering greater than 150 degrees. The 0.4-micrometer beam has the strongest forward scattering with fairly high backscattering. The 10.6-micrometer beam has the weakest forward scattering with fairly low backscatter. It may seem that the smaller wavelengths should have forward and backscattering strengths that are close to being equal because of Rayleigh scattering, but these graphs are a result of aerosols, not molecules. Aerosols are much larger than molecules, so these graphs are a result of Mie scattering from these aerosols. Each graph behaves differently because there are different types of aerosols at these different locations. HELEEOS also outputs the amounts and sizes of these aerosols in its Atmospheric Parameters Table. These are displayed below in Table 3.

Table 3: Aerosol sizes and amounts for Wright-Patterson Air Force Base, Caracas, Thule Air Base, and Kuwait

	Wright-Patterson AFB				Kuwait		
	Rmin (um)	Rad (um)	Rmax (um)		Rmin (um)	Rad (um)	Rmax (um)
insoluble - 0.1499 parts/cm ³	0.005	0.471	20	mineral (nuc) - 197.9 parts/cm ³	0.005	0.07	20
mineral (tra) - 4.999 parts/cm ³	0.02	0.5	5	mineral (acc) - 20.07 parts/cm ³	0.005	0.39	20
soot - 1840 parts/cm ³	0.005	0.0118	20	soot - 6941 parts/cm ³	0.005	0.0118	20
water soluble - 5615 parts/cm ³	0.0060008	0.02621	25.005	water soluble - 6641 parts/cm ³	0.005236	0.022377	21.1773
	Thule AB				Caracus		
	Rmin (um)	Rad (um)	Rmax (um)		Rmin (um)	Rad (um)	Rmax (um)
insoluble - 0.01998 parts/cm ³	0.005	0.471	20	insoluble - 0.24 parts/cm ³	0.005	0.471	20
sea salt (acc) - 1.908 parts/cm ³	0.0084463	0.37518	36.0245	soot - 200 parts/cm ³	0.005	0.0118	20
soot - 529.6 parts/cm ³	0.005	0.0118	20	water soluble - 4000 parts/cm ³	0.007072	0.034507	34.6374
water soluble - 518.5 parts/cm ³	0.0063731	0.02835	27.2388				

These aerosol tables relate to the four graphs in Figure 6. Notice that these aerosols are split up by the categories of water soluble, insoluble, mineral, sea salt, and soot. The amounts of each type of aerosol are displayed in parts/cm³ along with the sizes of each type of aerosol. R_{min} is the minimum radius size for that type of aerosol, R_{ad} is the modal

radius size, and R_{\max} is the maximum radius size for that type of aerosol. Each location differs significantly in the amount and types of aerosols for that site, as dictated by the Global Aerosol Dataset within HELEEOS.

Intensity and Irradiance

All of the intensity (or radiance) values in this thesis are in units of $\text{Wm}^{-2}\text{sr}^{-1}$. The irradiance coming from the platform (called “exitance” at the laser aperture) is consistent throughout. The variables include the laser geometry setup, the laser wavelength, and the atmospheric parameters. The research analyzes the propagation of a high-energy laser that produces 50,000 Watts. The aperture of this laser has a diameter of 0.5 meters. Since exitance has the units of Wm^{-2} it is given by the following equation,

Equation 17: Exitance

$$Ex = \frac{50,000\text{Watts}}{\pi \left(\frac{0.5\text{meters}}{2} \right)^2}$$

which is equal in this case to $254,647 \text{ Wm}^{-2}$. The steradian in the intensity measurement means that the electromagnetic waves are coming from a specific direction.

Scenario 1

In the first scenario analyzed, which is shown below in Figure 7, the platform at an altitude of 3,000 meters is beaming the 50,000-Watt laser to a target on the ground (altitude of 3,000 meters) directly below it.

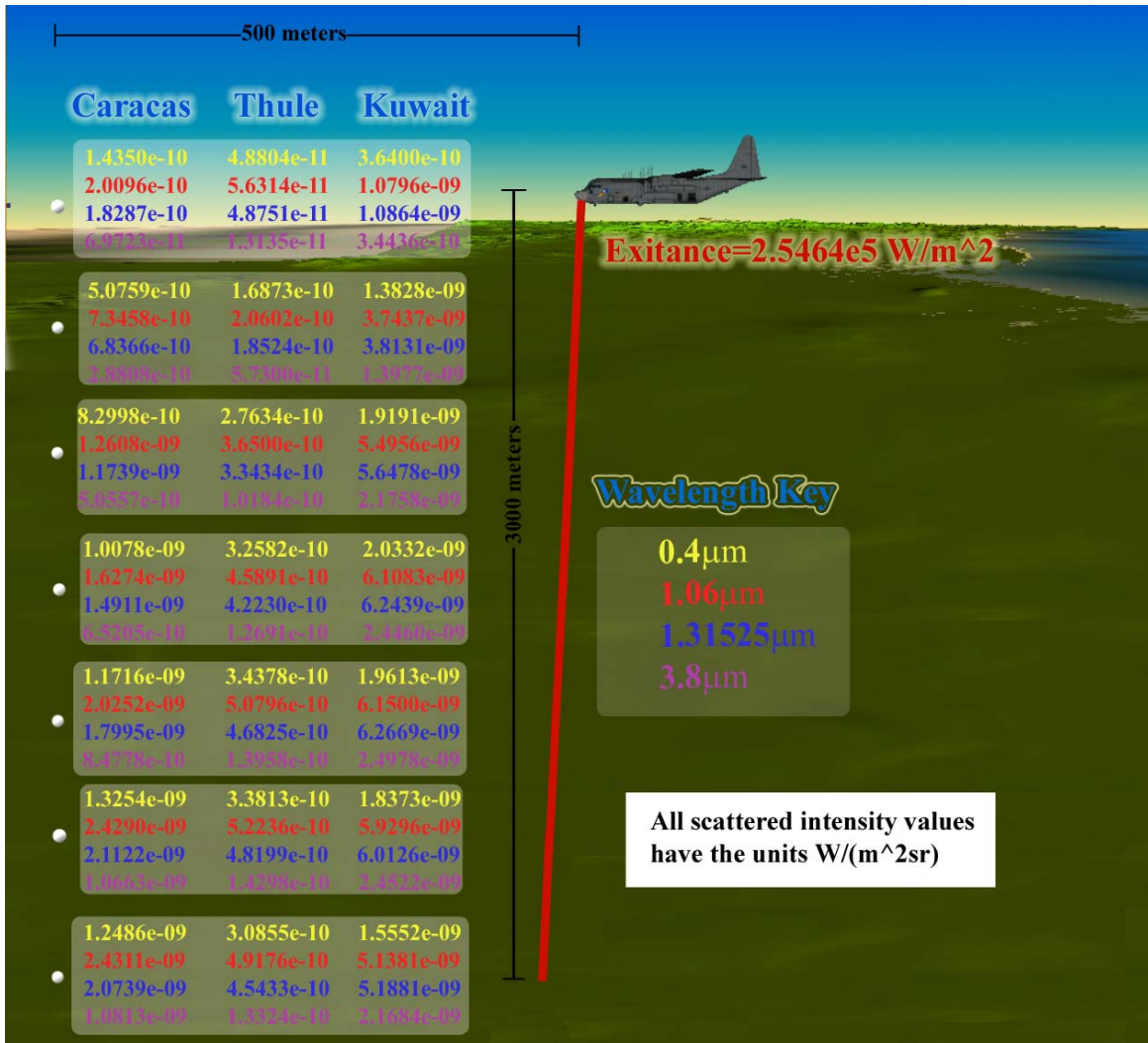


Figure 7: Scenario #1 Plane shooting laser straight down

In this scenario, the target and background are irrelevant because only scattering from the beam is taken into account, scattering and reflection from other sources are ignored. There are seven points that are placed at 500 meters north of the platform. It is assumed that the laser beam is always being shot north (azimuth of zero degrees) or the orientation of the platform is due north. Everything is in relation to the location of the platform, so if the off-axis observing point were 745 meters north and 484 meters east the azimuth

would be 32.9 degrees. These seven points all have the same ground distance of 500 meters from the platform and they are all at different altitudes. The first one is at an altitude of zero and the last one is at an altitude of 3,000 meters and they are all in increments of 500 meters. There are four different wavelengths that are being tested, 0.4 micrometers, 1.06 micrometers, 1.31525 micrometers, 3.8 micrometers. This same scenario tested for the locations of Caracas, Thule, and Kuwait, which gives a total of 84 different off-axis intensity values when combined with the atmospheres and wavelengths.

The scattered intensity values in Figure 7 behave as expected. In general the scattered intensity values are about 15 orders of magnitude smaller than the intensity values within the HEL beam. The intensity values at 3,000 meters are smaller than the values at zero meters because forward scattering is much greater than backscattering. Intensity values peak at different altitudes depending on the wavelength and atmosphere combination. For example, the wavelength of 1.06 micrometers peaks at zero meters in Caracas, the wavelength of 1.31525 micrometers peaks at 500 meters in Thule, the wavelength of 1.31525 micrometers peaks at 1,000 meters in Kuwait, and the wavelength of 0.4 μm peaks at 1,500 meters in Kuwait. These peak intensities at different altitudes are a result of various phase functions that can be seen in Figure 6 and of different absorption rates that can be seen in Figure 1.

Scenario 2

Below, Figure 8 is a scenario that is similar to the one in Figure 7.

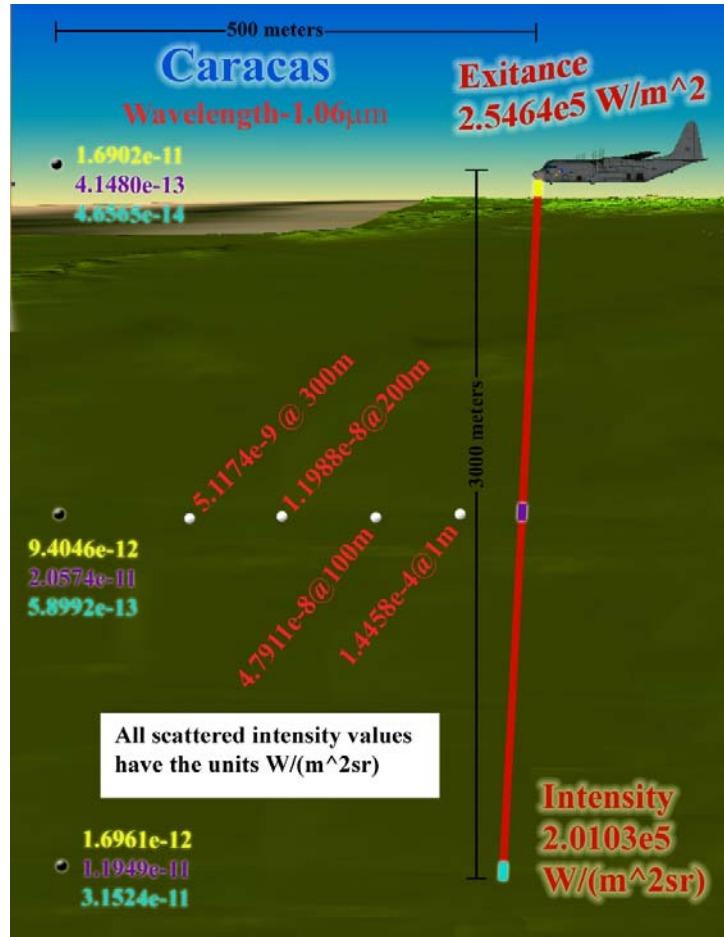


Figure 8: Scenario #2 Plane shooting laser straight down

This above scenario examines the Caracas scenario intensity values to identify the extinction effects between the beam and observer. The four white points on this image are at an altitude of 1,500 meters. They are at 300 meters, 200 meters, 100 meters, and one meter away from the beam. The point that is one meter away from the beam has an intensity of $1.4458e-4 \text{ Wm}^{-2}\text{sr}^{-1}$. Comparing this point to the intensity in the beam coming from the platform, there is a difference of approximately 9 orders of magnitude. The irradiance on target has the same order of magnitude as the exitance leaving the platform because the engagement has a transmission of almost 80%. The intensity values

at the observing points in Figure 8 range from $1.6274e-9 \text{ Wm}^{-2}\text{sr}^{-1}$ at 500 meters from the beam to $1.4458e-4 \text{ Wm}^{-2}\text{sr}^{-1}$ at one meter from the beam and do not increase linearly due to non-linear extinction. The closer the observing point is to the beam the more sensitive it is to a change in location. In other words, the intensity value increases faster as it gets closer to the beam. Figure 8 also shows three points that have the same locations as in Figure 7. These points are at the altitudes of zero meters, 1,500 meters and 3,000 meters. The Figure 8 intensities at these points differ from the Figure 7 intensities because they are displaying intensity coming from three separate sections of the beam rather than from 100 segments of the beam. In Figure 8, the intensity values that are coming from the 1st, 50th, and 100th segment are being displayed separately for each of these points. The top number corresponds to the scattered intensity from the segment that is exiting the laser, the middle number corresponds to the segment in the middle of the beam, and the bottom number corresponds to the segment that is closest to the target. These numbers are also color coordinated with the segments of the beam they represent.

By reviewing the intensity values at 3,000 meters in Figure 8, it is evident that the most scattering is coming from the platform segment (the terms platform segment, middle segment, and target segment to refer to that corresponding segment of the beam), and a very small amount is coming from the target segment. Looking at the point at 1,500 meters, it behaves a little differently than expected. This point receives highest intensity value from the middle segment, but it seems as though there would be more coming from the platform segment and the target segment. In reality, there is more intensity coming from these segments. Additional scattering and absorption due to the

longer path length to the observing point causes these values to be less than the middle segment value. The same concept is true for the point at zero meters. In light of the forward scattering nature of aerosols, the highest intensity value should be coming from the platform segment, but this is the lowest. The highest scattered intensity value is from the target segment because of the shorter path length to the observer. The distance to the target segment is 500 meters and the distance to the platform segment is a little more than 3,000 meters.

Extinction from the beam to the observer and scattering phase functions are the reasons that the intensity values behave the way that they do in Figure 9 and Figure 10. Scattering phase function graphs are already shown in Figure 6 and Figure 7, so now absorption is examined. Referring back to Figure 1, H₂O is the greatest molecular absorber. Therefore, atmospheres with different absolute humidity values have strong effects on the off-axis intensity values. This can be seen well in Figure 7 with the peak irradiance values occurring at different altitudes for tropical-humid Caracas, polar-dry Thule, and desert-moderate humid Kuwait.

Relative humidity, a factor that affects the size distribution of many aerosols and therefore modulates extinction due to scattering, is shown for various model atmospheres in Figure 9 to give an example of how relative humidity behaves in different environments. Only summer atmospheres are displayed for simplicity. All the atmospheres have been generated with the continental average for aerosols. The tables for these graphs are generated by HELEEOS, and show the various relative humidity levels at altitudes ranging from 3,000 meters down to zero meters.

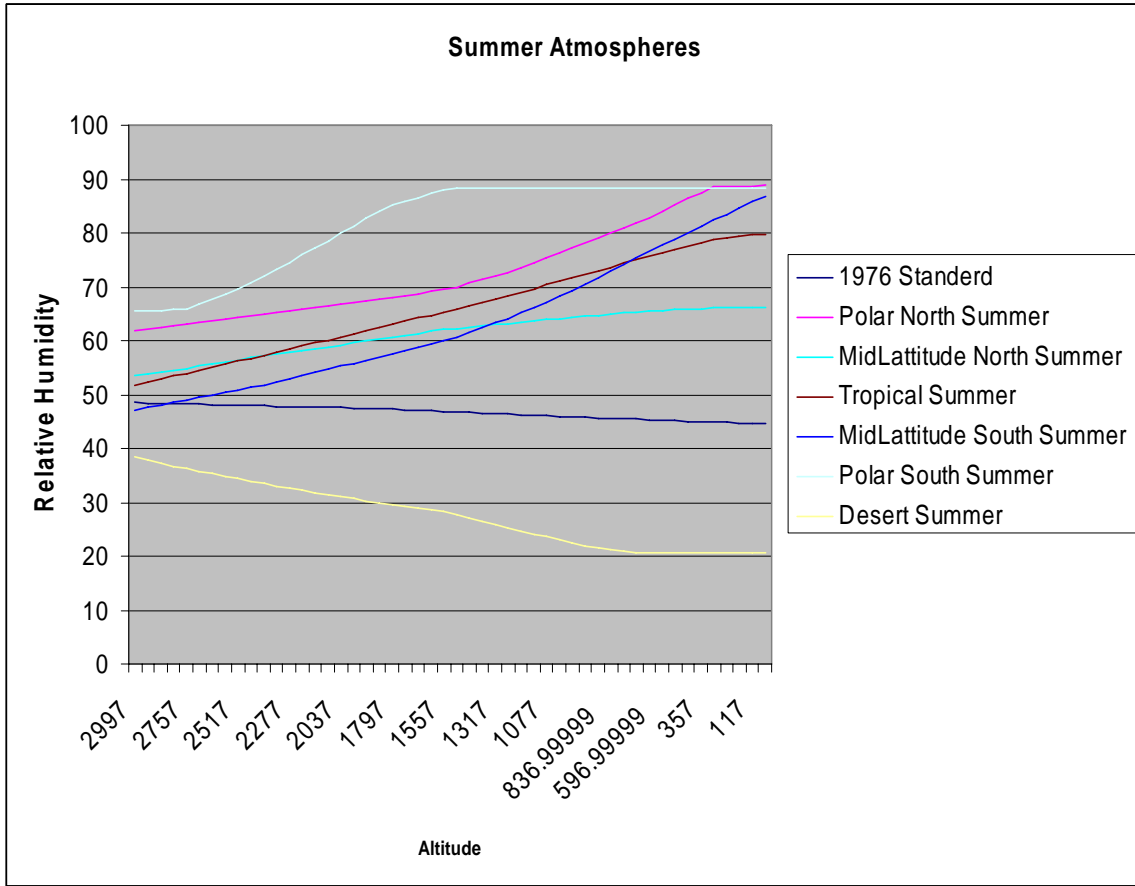


Figure 9: Relative Humidity

Scenario 3

The next scenario that is analyzed, which is shown below in Figure 10, compares the behavior of engagements in different altitudes.

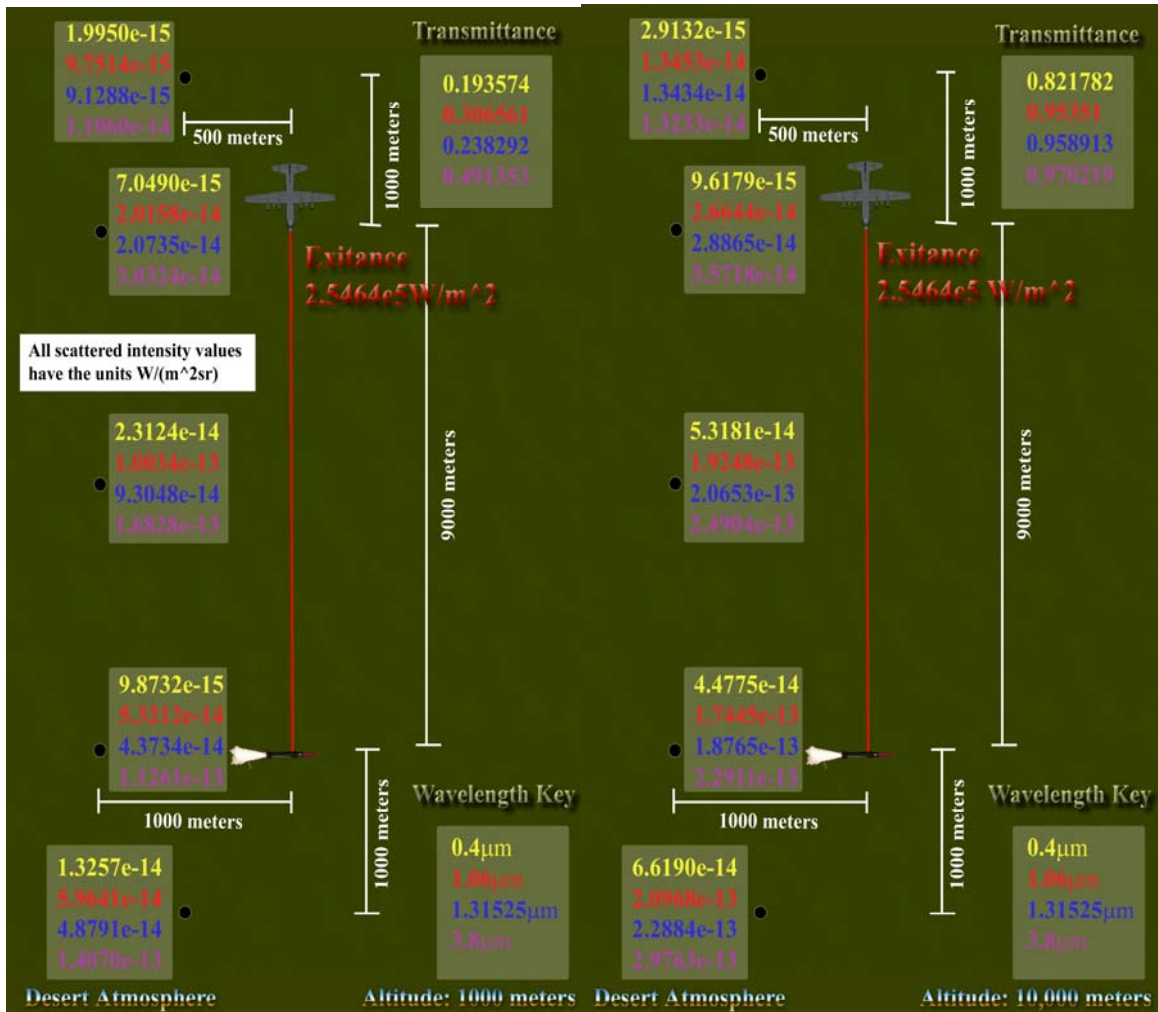


Figure 10: Scenario #3 Plane shooting laser horizontally

The scenario on the left occurs entirely at an altitude of 1,000 meters and the scenario on the right occurs entirely at an altitude of 10,000 meters. Both of these engagements have the same laser orientation, slant range, and off-axis scattered intensity observing points. There are 5 off-axis points all at the same altitude. The first point is 1,000 meters behind and 500 east of the platform. The next three points are 1,000 meters east of the platform and are aligned with the beginning, middle, and end of the laser beam being analyzed. The last point is 10,000 meters in front of the platform (1,000 meters beyond the target)

and 500 meters east of the platform. The center off-axis observing point in this scenario has the peak intensities because it has the largest field-of-view of the beam. It receives forward scattering from one end of the beam, side scatter from the middle of the beam, and backscatter from the other end of the beam. Since off-axis extinction is relatively strong at this low altitude, the side scatter from the middle of the beam is the strongest. The observing point with the second strongest scattered intensities is the point just beyond the target because forward scattering is strong. However, the scenario on the right (at 10,000 meters), has peak scattered intensities at a different point. Here, it is at the point just beyond the target because there is less off-axis extinction at the higher altitude due to fewer aerosols. According to the scattering phase function curve, forward scattering is much greater than side scattering causing these points to behave a little bit more like they would if there were no off-axis extinction. The second highest intensity point is in the middle of the beam as a result of the smaller amount of extinction that exists at this high altitude. The transmittance values at 1,000 meters range from 19%-49% and the transmittance value at 10,000 ranges from 82%-97%.

Scenario 4

The scenario, shown in figure 11, is the same scenario as in Figure 10, but with the off-axis observing points much closer.

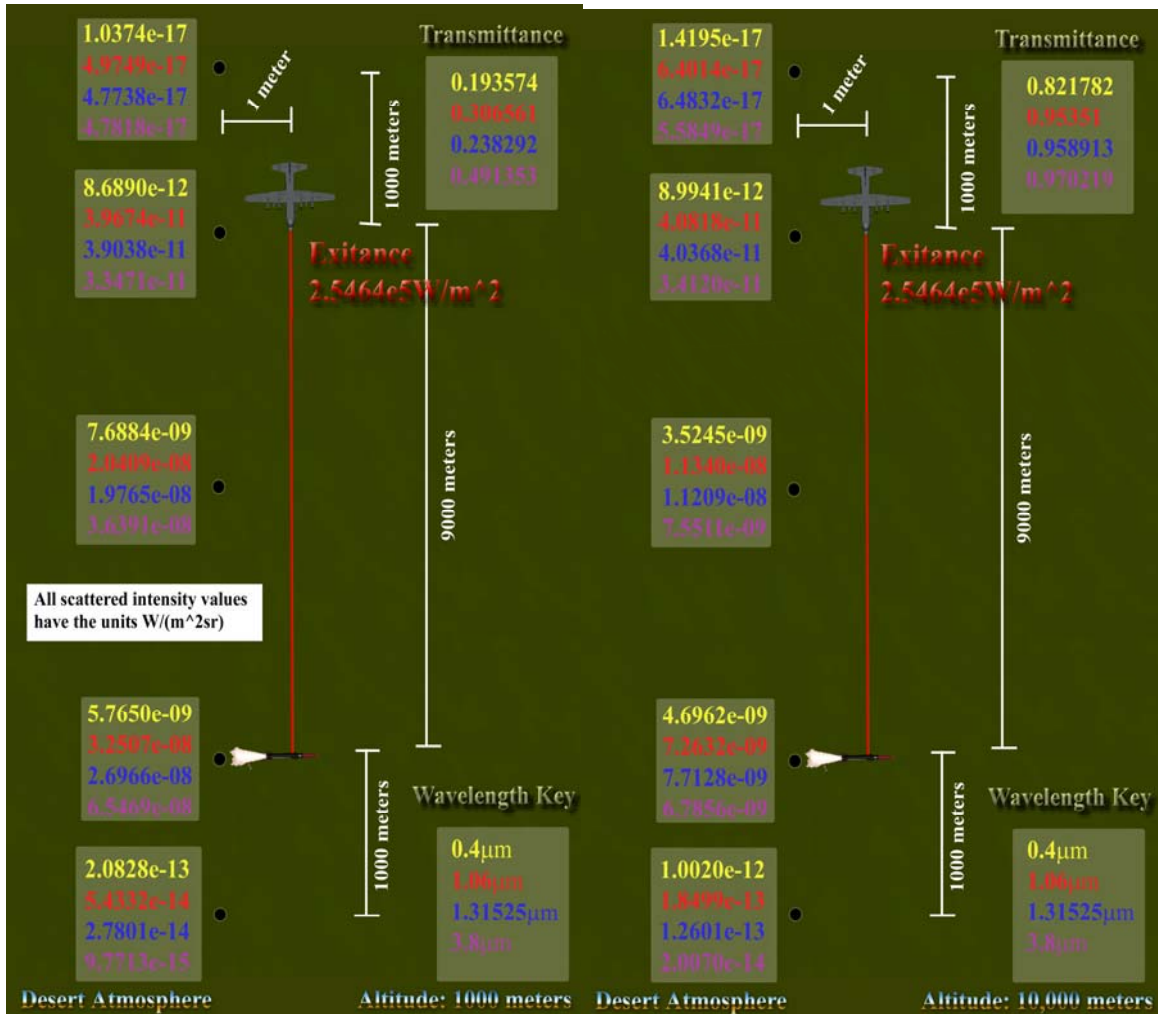


Figure 11: Scenario #4 Plane shooting laser horizontally-close

These points all have the same northing coordinates but now they are all just one meter east of the platform. The intensities in these scenarios are quite different than those in Figure 10. They are behaving the same in terms of forward scattering being larger than backscattering. The difference is at the points aligned with the beam. Here, the values are stronger at the midpoint and the target at the lower altitude, whereas in scenario #3 they were stronger at the higher altitude. This is a result of the points being so close to the beam that there is not much extinction taking place. The values at the observing

points nearest the target may initially seem incorrect. There are slightly higher values at the 10,000-meter altitude than at the 1,000-meter altitude. This is primarily due to the forward off-axis scattering from the length of the beam being less attenuated in the path to the observing point in the 10,000 meter case.

Figure 12, below displays intensity values for five different atmosphere types, six different geometries, and eight different wavelengths. Table 4 shows the geometric inputs and atmospheric inputs for Figure 12.

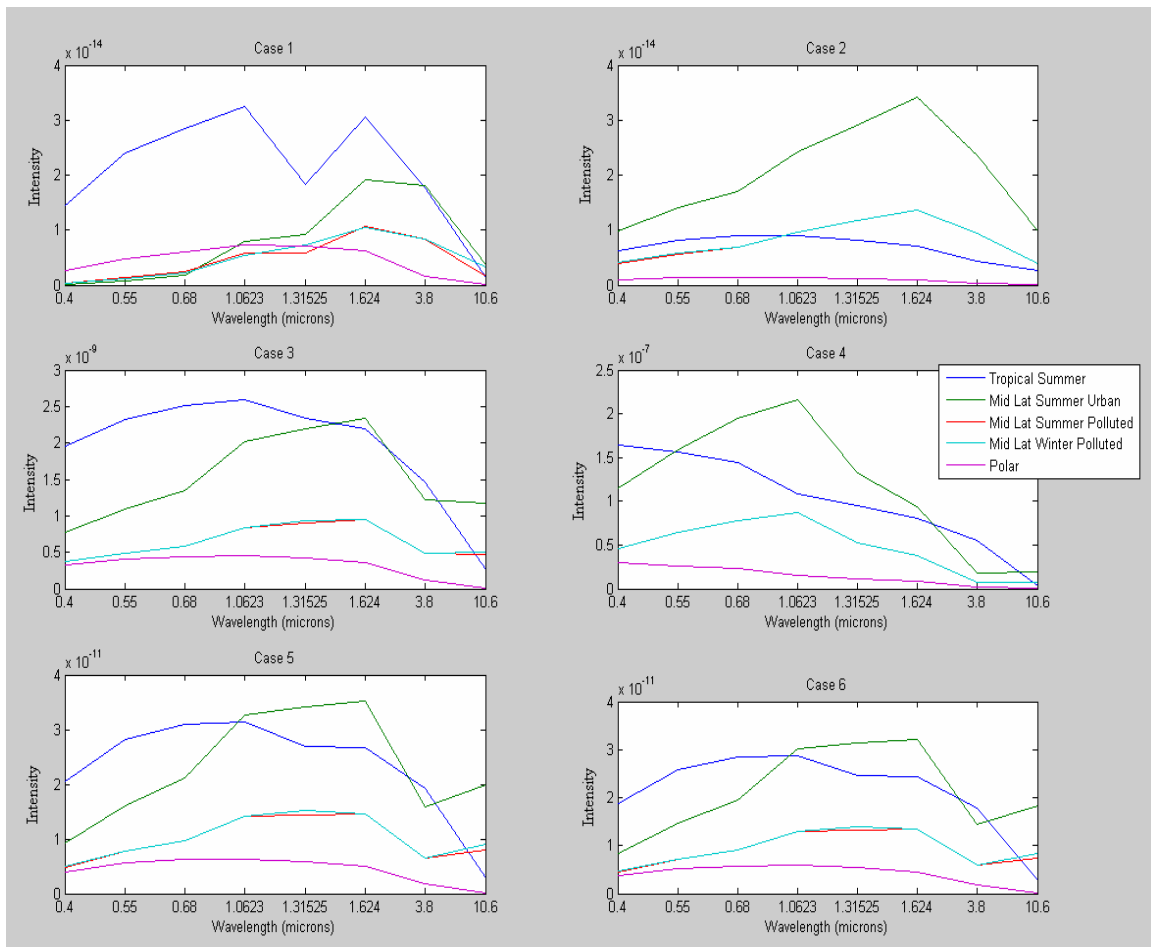


Figure 12: Intensity chart

Table 4: Reference table for Figure 12

Case	Laser Altitude	Target Altitude	Observer Altitude	Laser Slant Range	Observer Azimuth	Observer Slant Range	Observer Location
1	1,000	1,000	1,000	9000	2.86	10012.49	500m E 10km N
2	10,000	10,000	10,000	9000	2.86	10012.49	500m E 10km N
3	3,000	0	1,500	3,000	90	1581.13	500m E 0m N
4	5000	0	5005	8602	0	5	0m E 0m N
5	5000	0	5000	8602	0	7000	0m E 7000m N
6	5000	0	5000	8602	8.13	7071.06	1km E 7km N

Atmosphere Type	Aerosol Type	Site id	Percentile	Time of Day	Use Clouds	Cloud Type	Cloud Upper Altitude	Cloud Lower Altitude
6	8	0	5	9	0	1	0	0
4	2	0	5	9	0	1	0	0
4	5	0	5	9	0	1	0	0
5	5	0	5	9	0	1	0	0
3	9	0	5	9	0	1	0	0

The various numbers in Table 4 all represent specific input parameters. The input parameters that relate to these various numbers can be found in the atmospheric reference table, which is Table 8 located in Appendix A. Case 1 and 2 both have a laser being shot horizontally with a slant range of 9,000. The observing points in both cases are 500 meters east and 10,000 meters north (1,000 meters past the target). Case 1 occurs entirely at an altitude of 1,000 meters and Case 2 occurs entirely at an altitude of 10,000 meters. Case 3 has the platform shooting the laser straight down from an altitude of 3,000 meters. The observing point in the case 3 is 500 meters north at an altitude of 1,500 meters (same geometric set-up as Figure 4). Case 4, 5, and 6 are cases where the platform is at an altitude of 5,000 meters shooting a target 7,000 meters north (slant range of 8,602 meters). Each of these three cases has the observing point in a different location viewing the same beam. Case 4 has a pilot's view being five meters above the exit location of the laser beam. Case 5 has the observing point directly above the target at the same altitude

of the platform. Finally, Case 6 is the same as Case 5 but the observing point is 1,000 meters east.

By reviewing Figure 12, one can see that altitude plays a large role in the amount of scattered intensity observed at different altitudes. This can be seen in Case 1 and 2 by examining the Tropical Summer and Mid-Latitude Summer curves. At the lower altitude Tropical Summer has the strongest scattered intensities, and at the higher altitude Mid-Latitude Summer has the strongest scattered intensities. The Polar location has the least amount of scattering for all cases. The strongest scattered intensities are seen in Case 4, which is the amount of scattered intensity that reaches the point where the pilot is generally located.

Figure 15 through Figure 29 have the same geometry set-up as Figure 12. Due to repetitiveness of these figures, they are located in Appendix A. Each figure has different atmospheric parameters that can be found in the tables just below each of these figures. Table 8, the Atmospheric Reference Table, is also in Appendix A and is useful in interpreting Figure 15 through Figure 29.

Clouds

Cloud droplets strongly scatter HEL beams and at the same wavelengths, can be significant absorbers as well. Generally the scattering effects are several orders of magnitude greater than the absorption effects. Figure 13 shows the scattering phase function for a 1.31525 micrometer laser in a desert scenario with desert aerosols. The lower three curves show the scattering phase function for a cumulus continental clean

cloud at the given wavelength. The top three curves show the cloud free, scattering phase function (aerosols only).

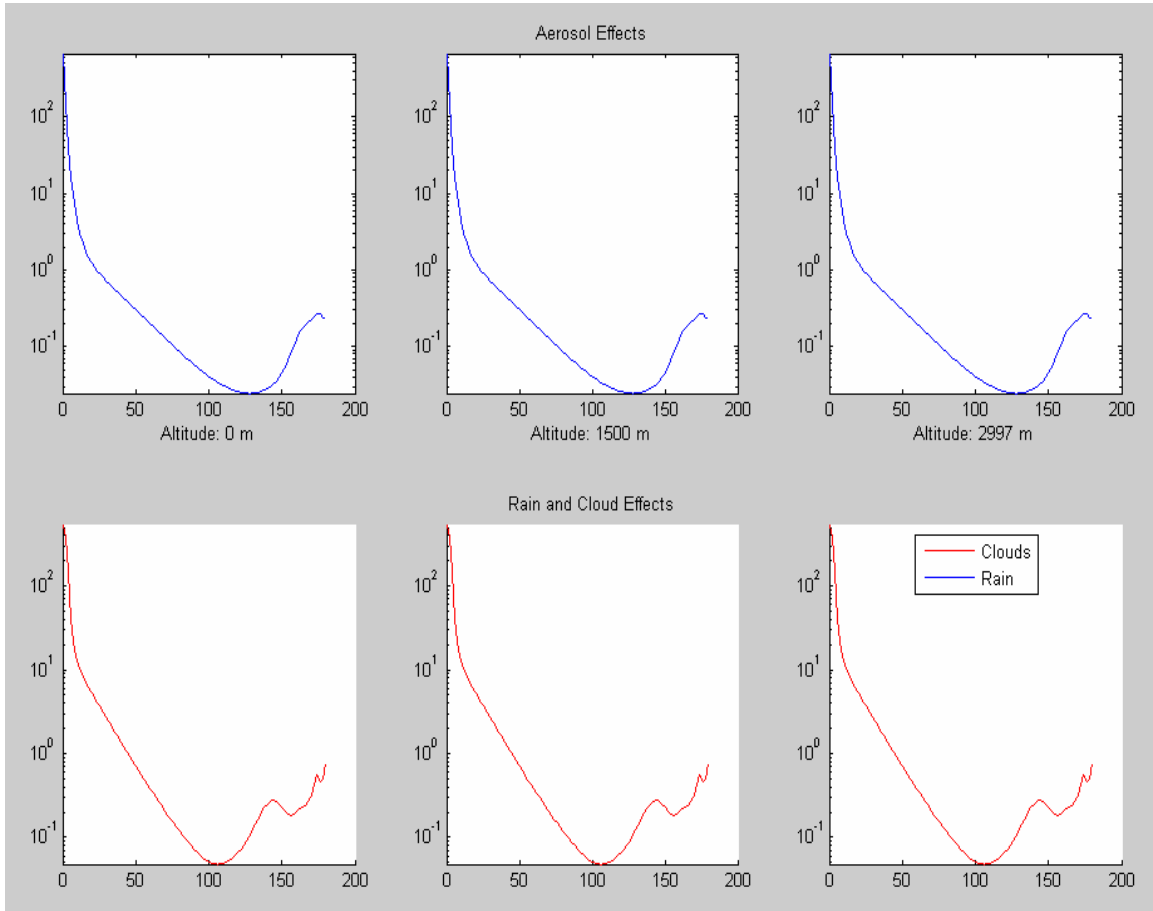


Figure 13: Scattering phase function for cumulus clouds at 1.31525 micrometers

Note that the minimum amount of side scattering is at a different phase angle for the clouds and aerosols. The minimum amount of side scattering for the cloud is roughly 105 degrees, and the minimum amount of side scattering for the aerosols is roughly 130 degrees. The curve displayed for the cloud is a bit more complex, with more fluctuations than just the aerosols alone.

Figure 15 and Figure 16 (Appendix A) compare the behavior of a laser beam propagating through different types of clouds. Figure 15 has stratus clouds set up from 1,600 meters down to 999 meters and Figure 16 has cumulus continental clean clouds set up from 1,600 meters down to 999 meters. The reason 999 meters was chosen for the lower cloud altitude is to ensure the entire laser path is within the modeled cloud. Table 7, also located in Appendix A, shows the geometric set-up for Figure 15 through Figure 29. The off-axis observing point for Case 1, 2, and 3 are actually located in the cloud and the others are not. For the most part, cumulus clouds and stratus cloud behave very similarly. Comparing Figure 15 and Figure 16, it can be seen that there are only two cases where these clouds behave differently. Case 3 has more off-axis intensity at 10.6 micrometers for the cumulus cloud and exhibits slight differences in the wavelengths of Case 4. The larger cumulus droplet size distribution causes more off-axis scattering at 10.6 micrometers. Note that in Case 3 the observer point is to the side of the laser beam and in Case 4 the observer point is behind the laser beam.

Clouds vs. Fog

Fog is a cloud in contact with the ground. It is modeled like clouds but with a lower number density and different droplet size distribution. Figure 17 is a fog scenario similar to the cloud scenario. The fog exists between the altitudes of 999 meters and 1,600 meters, so in this case fog is treated like a different type of cloud. It can be seen that the fog in Figure 17 has higher off-axis intensity values for Cases 1 and 3 and lower intensity values for all of the other cases. The primary reason for this is Cases 1 and 3 have geometries that allow the lower number density of fog droplets to attenuate the off-

axis intensity less. In Case 2 at a higher altitude, the behavior is similar except scattered intensity values for clouds are slightly higher. Fog allows significantly more transmittance than a cloud. Clouds have very high scattering characteristics, with little or no transmittances over paths greater than one kilometer .

Fog vs. Rain

Figure 18 is a fog scenario again, but this time it has been run for comparison with rain. Here, it runs from an altitude of 10,001 meters down to the ground. The reason why the altitude of 10,001 meters was chosen was to ensure that Case 2 was in fog. Figure 19 through Figure 23 analyze rain from 10,001 meters down to the ground in the same manner. By looking at Figure 18 and comparing Case 1 and 2, one can see that at a very high altitude all geographic locations behave very similarly. Nevertheless, at lower altitudes there tends to be more of a difference in behavior due to the larger amount of scatterers (rain drops, droplets, aerosols, and molecules) at these lower altitudes. Case 4 shows that the amount of backscatter behaves the same for all locations. Each case has the tendency to decrease as the wavelength increases for rain, but for fog each case has the tendency to increase. On the other hand, at 10.6 micrometers the scattered intensity goes to zero in both cases. This is caused by the increased amount of absorption by liquid H₂O at this wavelength. Looking at Case 1, it can be seen that fog has almost no forward scattering at low altitudes. Comparing this to rain, there is a big difference. Rain also has a low amount of forward scatter but it is much stronger than the forward scatter for fog. Case 4 shows that the backscatter for fog is higher than the backscatter for extreme rain. Rain is similar to fog in the aspect that forward scattering behaves

differently at lower altitudes and similarly at higher altitudes. Also, backscatter behaves similarly for all locations.

Rain

The scattering phase function for rain can be seen below in Figure 14.

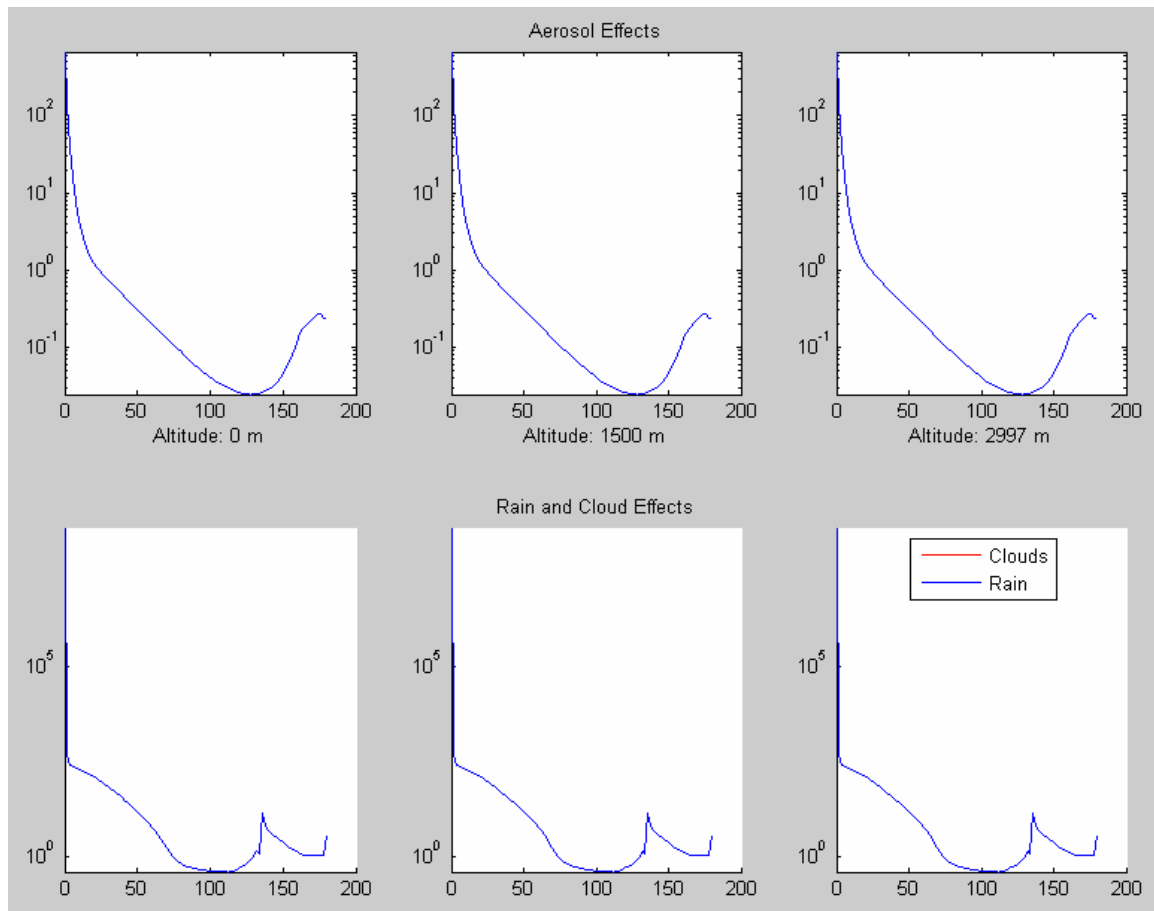


Figure 14: Scattering phase function for rain

The rain scattering function behaves in some ways like that for cumulus clouds. Like clouds, rain has minimum side scatter at a phase angle of about 105 degrees. Also, like clouds, rain has a peak in scattering phase function at about 140 degrees. Major

differences include the strength of the forward scatter peak for rain and the sharp rainbow feature at 137 degrees. With the exception of the forward scatter peak, the scattering phase function for rain can be predicted with geometric optics (ray tracing).

Very light rain corresponds to a rain rate of 2 mm/hr, light rain corresponds to a rain rate of 5 mm/hr, moderate rain corresponds to a rain rate of 12.5 mm/hr, heavy rain corresponds to a rain rate of 25 mm/hr, and extreme rain corresponds to a rain rate of 75 mm/hr. As the rain rate increases from light to extreme, scattered intensity values decrease for Cases 1, 2, 5, and 6. This is logical because these cases correspond to phase angles less than 90 degrees. In other words, they correspond to forward scattering from a distance. The distance causes the intensity values to attenuate as the rain rate increases. There is one case that has behavior that initially may seem odd. Case 3, for the most part, decreases as the rain rate increases but its peak value is not seen in the very light rain case. The peak value for this point is found in the light rain case. The reason for this is because the light rain case is the optimal point for this scenario. As the rain rate increases the amount of scattering from the laser beam increases causing more scattering in that specific direction. As this happens, the extinction increases between the beam and the off-axis point as well. Light rain has the perfect combination of scattering and extinction to allow the maximum amount of irradiance through to this point. Of course, if the point were moved closer, further away, or if the slant range of the beam was changed, the optimal amount of rainfall would be different as well. The optimal amount of rainfall could just as well be no rainfall at all. Case 4 shows that as the rain rate increases, the

amount of backscatter increases and as a result it always behaves the same for all locations.

Ocular Hazard Calculation

All off-axis intensity values in this entire thesis are in the units of $Wm^{-2}sr^{-1}$. The previous chapter states that the human eye can see $4/3\pi$ (4.1887) steradians and the diameter of a pupil can range from 1.5 mm and to 8 mm. Some of the MPE values in Appendix B are in Wcm^{-2} , but the majority of them are in Jcm^{-2} . The intensity values in this research must be converted from $Wm^{-2}sr^{-1}$ to Jcm^{-2} . First, the intensity values must be multiplied by 4.1887 steradians to remove the sr^{-1} . Next, meters are converted to centimeters. Now the values can be compared to the Wcm^{-2} MPEs in the table or they can be converted to joules. Since Watts are equal to joules per second, the dwell time of the engagement must be known. If for example if the dwell time is 10 seconds the intensity value would be multiplied by 10s. This would remove the seconds, changing the Watts to joules.

Below, Table 5 is calculated from the MPE equations in Table 24, and the proper correction factors in Table 27. The time used for the calculation of the MPE values as well as the maximum intensity values is 10 seconds. The maximum intensity values used are the largest backscatter values found in this research and they come from the cumulus cloud scenario, which is shown in Figure 16, Case 4. Note that Case 4 in Figure 15 through Figure 29 correspond to the pilot scenario with the observer just about the laser exit location.

Table 5: MPEs for ten seconds

Wavelength	MPE (J/cm²)	Max Irradiance Value (J/cm²)	
0.4 micrometers	1	1.5079e-1	Less
0.55 micrometers	1.0122e-2	1.2566e-1	More
0.68 micrometers	1.0122e-2	1.1728e-1	More
1.0623 micrometers	5.0611e-2	1.1309e-1	More
1.31525 micrometers	4.0488e-1	1.2566e-1	Less
1.624 micrometers	1	1.5498e-1	Less
3.8 micrometers	9.9583e1	7.5396e-2	Less
10.6 micrometers	9.9583e1	0	Less

Notice that there are three wavelengths that are larger than the recommended MPE values. Further note that the dwell time of this engagement is 10 seconds. The average dwell time for engagements is 4 seconds, so this is a worst-case scenario. The limiting aperture of the eye is not needed because it is calculated into the equations of the MPE values. It should also be expressed that the SSL and the COIL are at wavelengths in the non-visible range, but still reach the retina of the eye. Consequently, these lasers can be most harmful at night since the pupil is more likely to be fully dilated during this time.

Relative Humidity

These eight wavelengths, six geometries, and six locations were also run with three different relative humidity values. These three values consist of the 1st (driest),

50th, and 99th (wettest) percentiles and can be seen in Figure 24 through Figure 26 in Appendix A. Throughout all geometries in the 1st percentile, Thule and Wright-Patterson AFB have the lowest intensity values. In Case 2 through Case 6, Cairo has the highest intensity values. In Case 1, Beijing has the highest intensity value. In Case 1, the intensity values for Beijing decrease as relative humidity increases. This leaves Caracas and Thule with the largest amounts of off-axis intensity. This is odd because all of the other geometry set-ups show Caracas and Thule as having very low intensity values.

Time of Day

The previous scenarios are also run for different times of day. These are shown in Figure 27 through Figure 29. Figure 27 represents 0000-0300, Figure 28 represents 0600-0900, and Figure 29 represents 1200-1500. These three figures have small changes; hence it is hard to see the variations between the graphs. The cause of these small changes is due to the varying height of the boundary layer during the different times of day.

Laser Pointer Test

The final simulation is for comparison to a visual laboratory test. The visual test consisted of two different lasers of equal power but different wavelengths. These lasers were ~5 milliwatts and included red and green wavelengths. A laser with the wavelength of blue light was not used in the test because of the rarity and high price of this type of laser. Both lasers were shot in a dark room with observers in different locations. The

observers could not see the red laser at any angle; however, the green laser could be seen. The beam of the green laser could be seen due to atmospheric Rayleigh scattering because this is more dominant at shorter wavelengths than Mie scattering. Mie scattering could be seen when dust particles floated through the beam. The backscattering of the green laser was easily seen. The side scattering was not seen until the eyes fully adjusted to the dark. The forward scattering was also easily seen and seemed slightly stronger than the backscattering intensity. The HELEEOS simulation consisted of five-milliwatt laser beams with aperture diameters of five millimeters and a slant range of 10 meters. Three observation points were used, which were all one meter east of the beam. The first point had the same northing coordinate as the platform, the second point was five meters north of the platform, and the third point was ten meters north of the platform.

The results of the laser pointer simulation are shown below in Table 6.

Table 6: Laser pointer simulation

	Blue Laser	Green Laser	Red Laser
Backscatter	4.0046e-13	3.07e-14	3.78e-15
Side-scatter	8.6666e-14	6.72e-015	9.02e-16
Forward-scatter	4.5641e-13	3.59e-014	5.44e-15

These numeric values agree with the visual tests that were previously conducted. It can be seen that the forward-scatter and backscatter values are all very close, but forward-scatter is still dominant. The stronger Rayleigh scattering is responsible for this. As seen in the visual test, the side scattering values are the lowest. It can also be seen that as the

wavelength gets longer, forward scattering is significantly stronger than the backscattering.

V. Conclusions and Recommendation

Conclusions of Research

This study demonstrates by computer simulation that critical information can be derived about HEL platform characteristics and the intended target via the measured off-axis scattered beam intensity. However, for this to be determined, the exact location of the platform and target must be known. This is not taking into account the additional scattering that would be caused by the laser beam interacting with the target (target reflection or BRFD). This also assumes that inversion techniques used to acquire the information are sensitive enough to distinguish the signal of the beam from the surrounding background noise. Such inversion calculation methods are suggested by this research, but not described herein. The lasers being observed consist of a single wavelength that would assist in distinguishing the signal from the noise. The exact atmospheric condition and time of day must be known. Combining this information with observed off-axis intensity, the exitance from a platform and the irradiance arriving at a target can be calculated. Such information is of paramount importance to the Laser Intelligence (LASINT) community depending in the classification level of the mission being conducted. This same concept, however, can work in the favor of the friendly forces if any opposing forces utilized HELs like those simulated in HELEEOS.

Under typical conditions, the scattered, off-axis intensities pilots would likely encounter are less than the MPE amounts set forth by ICNIRP. On the other hand, there are certain circumstances when the intensity values encountered by pilots exceed the recommended MPE values. The case encountered here, was in the situation of a pilot

flying above a cloud with the target being below the cloud, and the laser having a dwell time of 10 seconds. There may be many more situations that would produce off-axis intensity at elevated values, but it is very time consuming to test every possible combination of scenarios. The major constraint that was encountered was the runtime, which took 4 minutes per observation point calculated in clear atmospheric conditions. Initially, when rain and clouds were introduced, the runtime drastically increased to more than an hour per observation point calculated. By choosing a “select” wavelength with pre-calculated look-up tables the runtimes were dramatically reduced.

Significance of Research

There is an up-and-coming new technology of high-energy laser (HEL) weapon systems. These technologies are currently under development with extensive research taking place to rapidly deploy these new innovations. With these new technologies surfacing, a massive amount of new threats to safety as well as security emerge. The equations and software researched and demonstrated in this study allow a starting point for future researchers to quantify these safety and security threats.

Recommendations for Action

It is recommended that action be taken for the eye safety of the pilots of these HEL aircraft. Wearing goggles that reflect or absorb the specific wavelengths that the lasers emit would be effective. Perhaps even more effective would be aircraft windshields that restrict these wavelengths because goggles can be forgotten, misplaced, or just not worn. There is no action that can be taken to prevent enemies from

intercepting scattered rays for the use of inversion technique. However, people can be educated about these intervention techniques, just as people are educated about hackers and malicious computer viruses.

Recommendations for Future Research

There are a few possible areas for research to branch from the efforts conducted in this research. First there is target scatter or reflection, which is not taken into account here. The scattering values calculated are conservative, and could possibly be higher. Target scatter can possibly get complex with the large variety of different material combinations and substance mixtures there can be.

Another topic is the study of the signal-to-noise ratio (SNR), as this research has documented that the off-axis intensities are very small. It is difficult to receive a weak signal with clutter and background noise. Future research should seek to characterize the background noise and the threshold SNR.

The research conducted did not take into account the size of the pupil at the time of viewing of this scattered intensity. In bright light, the pupil can get as small as 1.5 mm and in dim light it can increase to the size of 8 mm. The part of the eye that this intensity enters may also be studied. Humans have a very small viewing angle that allows the focusing of light. As the viewing angle increases, the ability to focus this light decreases until peripheral vision is reached, which is where the focusing ability is at a minimum.

Multiple scattering is the effect of photons being scattered out of the original path of the laser beam and then being scattered back into the path. These calculations can become very complicated and would slightly increase the scattered intensities recorded.

Laser communications can be studied as well. Laser communication is transmitting data via laser beams. The purpose of this is for very highly secure data transmittal. This method is expected to be very secure compared to transmitting data by radio signal. With the scattering of the atmosphere and the proper inversion techniques based on the methods in this research, it may show laser communications to be less secure.

Finally, the Matlab code written in this research runs fairly slow. It needs to be optimized to run faster. One immediate way to increase the speed of runs is by decreasing the number of segments that the script currently analyzes. Decreasing the number of segments would improve time, but it would decrease the level of accuracy. A proper trade-off level between the two needs to be found.

Appendix A

Table 7: Geometric Reference Table

Case	Laser Altitude	Target Altitude	Observer Altitude	Laser Slant Range	Observer Azimuth	Observer Slant Range	Observer Location
1	1,000	1,000	1,000	9000	2.86	10012.49	500m E 10km N
2	10,000	10,000	10,000	9000	2.86	10012.49	500m E 10km N
3	3,000	0	1,500	3,000	90	1581.13	500m E 0m N
4	5000	0	5005	8602.32	0	5	0m E 0m N
5	5000	0	5000	8602.32	0	7000	0m E 7km N
6	5000	0	5000	8602.32	8.13	7071.06	1k E 7km N

Table 8: Atmospheric Reference Table

Atmosphere Type	Aerosol Type	Site ID	
3 – Polar North Winter 4 – Mid-Latitude North Summer 5 – Mid-Latitude North Winter 6 – Tropical Summer 16 – ExPERT Location	2 – Urban 5 – Continental Polluted 8 – Maritime Tropical 9 – Arctic 0 – N/A	16 – Thule 95 – Kuwait 145 – Beijing 157 – Cairo 253 – Wright-Patterson AFB 265 – Caracas 0 – N/A	
Percentile	Time of Day	Use Clouds	Cloud Types
1 – 1%(most dry)	1 – 0000-0300	0 – don't use clouds	1 – Cumulus Continental Clean
5 – 50%(average)	3 – 0600-0900	1 – use clouds	4 – Stratus Continental
9 – 99%(most damp)	5 – 1200-1500		6 – Fog
	9 – Daily Average		7 – Very Light Rain
			8 – Light Rain
			9 – Moderate Rain
			10 – Heavy Rain
			11 – Extreme Rain

Table 9: Stratus Continental Clouds

Atmosphere Type	Aerosol Type	Site id	Percentile	Time of Day	Use Clouds	Cloud Type	Cloud Upper Altitude	Cloud Lower Altitude
16	0	265	5	9	1	4	1,600	999
16	0	16	5	9	1	4	1,600	999
16	0	95	5	9	1	4	1,600	999
16	0	253	5	9	1	4	1,600	999
16	0	157	5	9	1	4	1,600	999
16	0	145	5	9	1	4	1,600	999

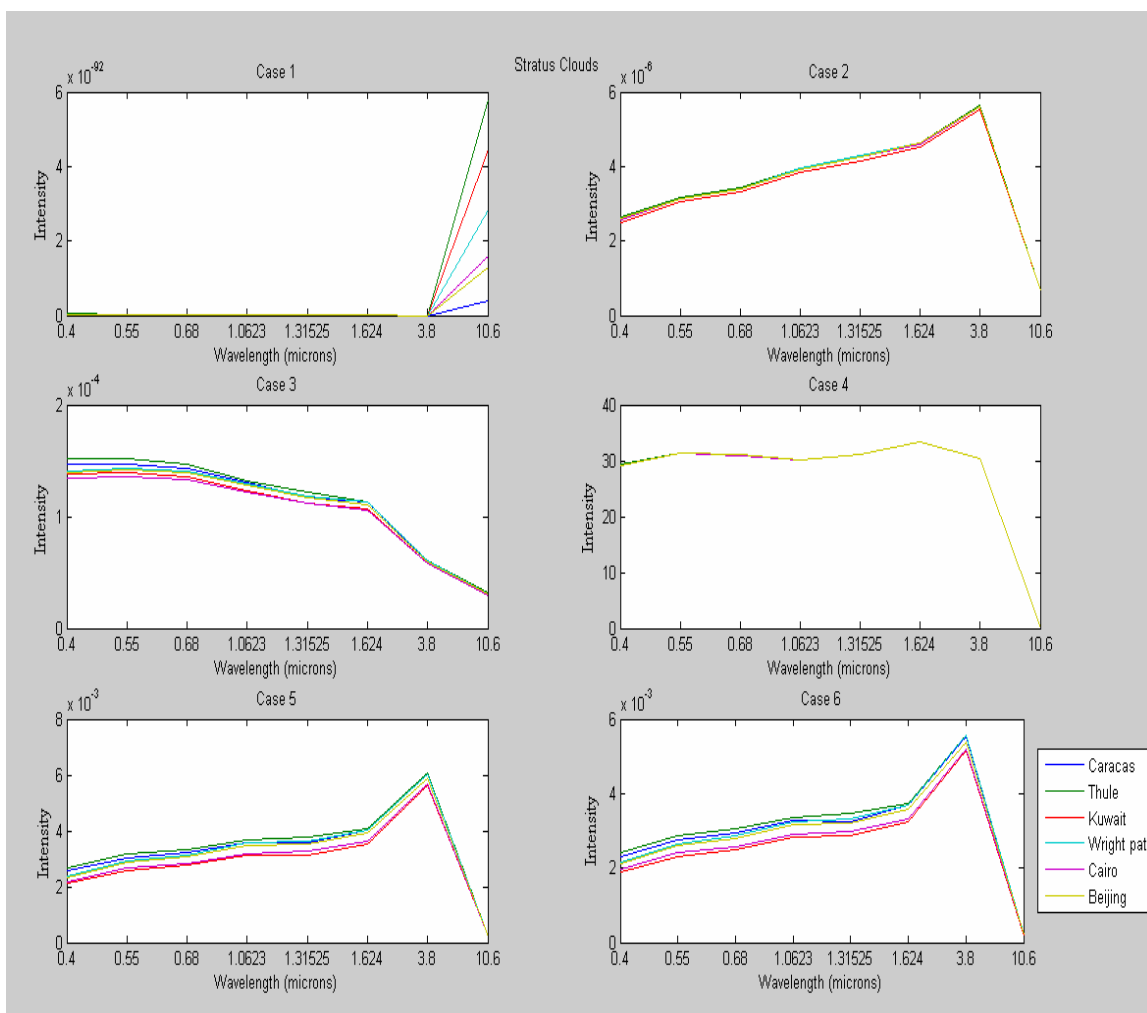


Figure 15: Stratus Continental Clouds

Table 10: Cumulus Continental Clean Clouds

Atmosphere Type	Aerosol Type	Site id	Percentile	Time of Day	Use Clouds	Cloud Type	Cloud Upper Altitude	Cloud Lower Altitude
16	0	265	5	9	1	1	1,600	999
16	0	16	5	9	1	1	1,600	999
16	0	95	5	9	1	1	1,600	999
16	0	253	5	9	1	1	1,600	999
16	0	157	5	9	1	1	1,600	999
16	0	145	5	9	1	1	1,600	999

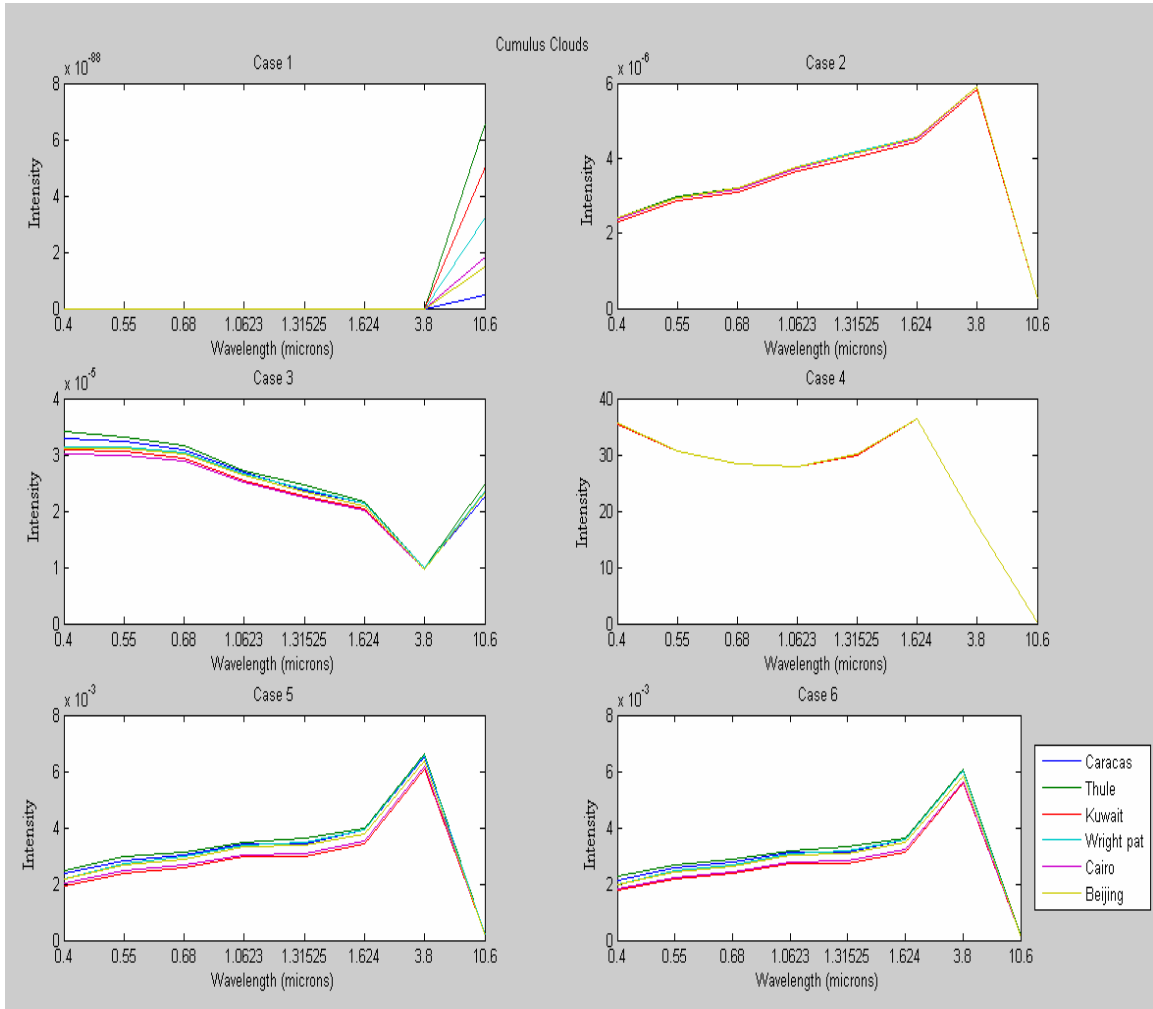


Figure 16: Cumulus Continental Clean Clouds

Table 11: Fog (1)

Atmosphere Type	Aerosol Type	Site id	Percentile	Time of Day	Use Clouds	Cloud Type	Cloud Upper Altitude	Cloud Lower Altitude
16	0	265	5	9	1	6	1,600	999
16	0	16	5	9	1	6	1,600	999
16	0	95	5	9	1	6	1,600	999
16	0	253	5	9	1	6	1,600	999
16	0	157	5	9	1	6	1,600	999
16	0	145	5	9	1	6	1,600	999

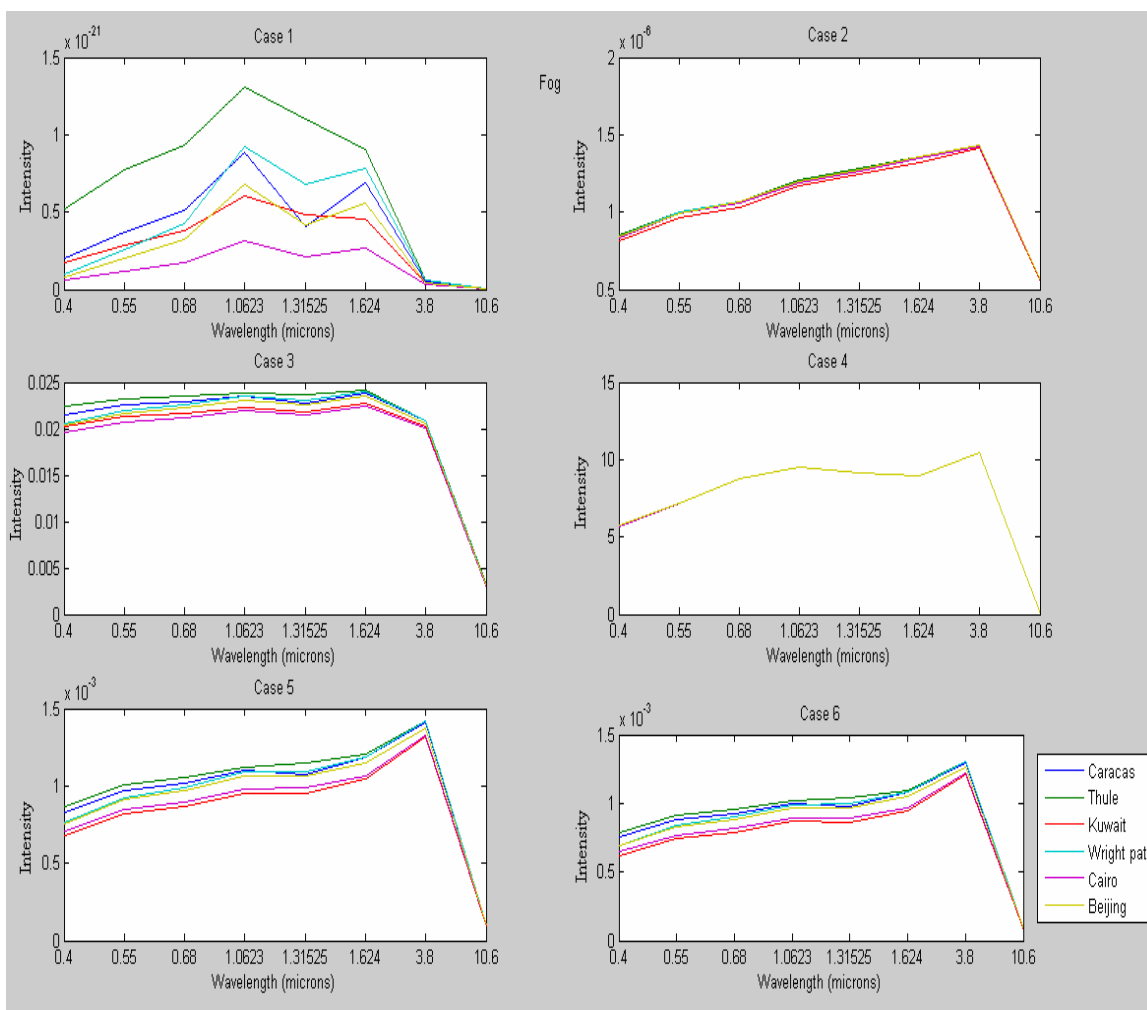


Figure 17: Fog (1)

Table 12: Fog (2)

Atmosphere Type	Aerosol Type	Site id	Percentile	Time of Day	Use Clouds	Cloud Type	Cloud Upper Altitude	Cloud Lower Altitude
16	0	265	5	9	1	6	1,0001	0
16	0	16	5	9	1	6	1,0001	0
16	0	95	5	9	1	6	1,0001	0
16	0	253	5	9	1	6	1,0001	0
16	0	157	5	9	1	6	1,0001	0
16	0	145	5	9	1	6	1,0001	0

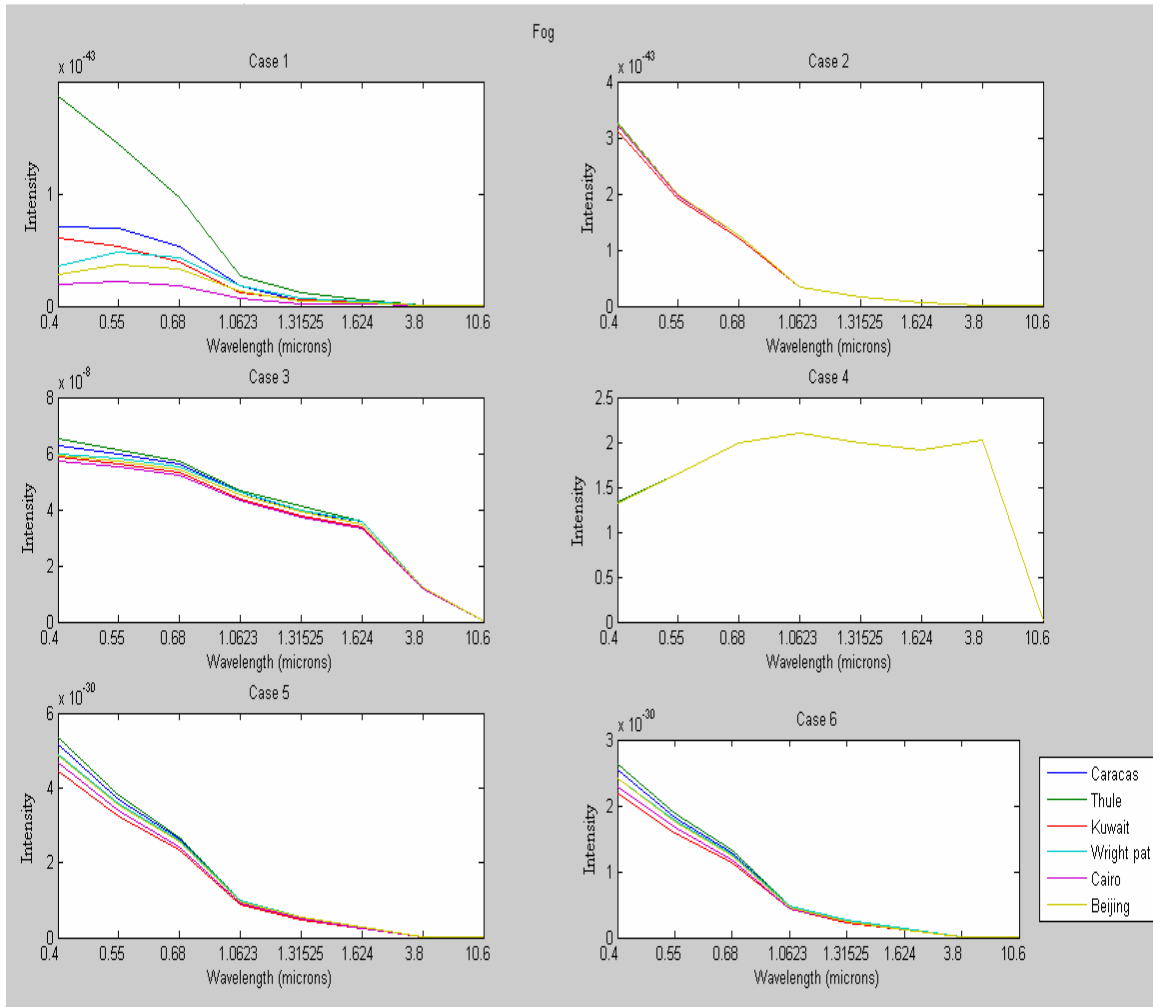


Figure 18: Fog (2)

Table 13: Very Light Rain

Atmosphere Type	Aerosol Type	Site id	Percentile	Time of Day	Use Clouds	Cloud Type	Cloud Upper Altitude	Cloud Lower Altitude
16	0	265	5	9	1	7	1,0001	0
16	0	16	5	9	1	7	1,0001	0
16	0	95	5	9	1	7	1,0001	0
16	0	253	5	9	1	7	1,0001	0
16	0	157	5	9	1	7	1,0001	0
16	0	145	5	9	1	7	1,0001	0

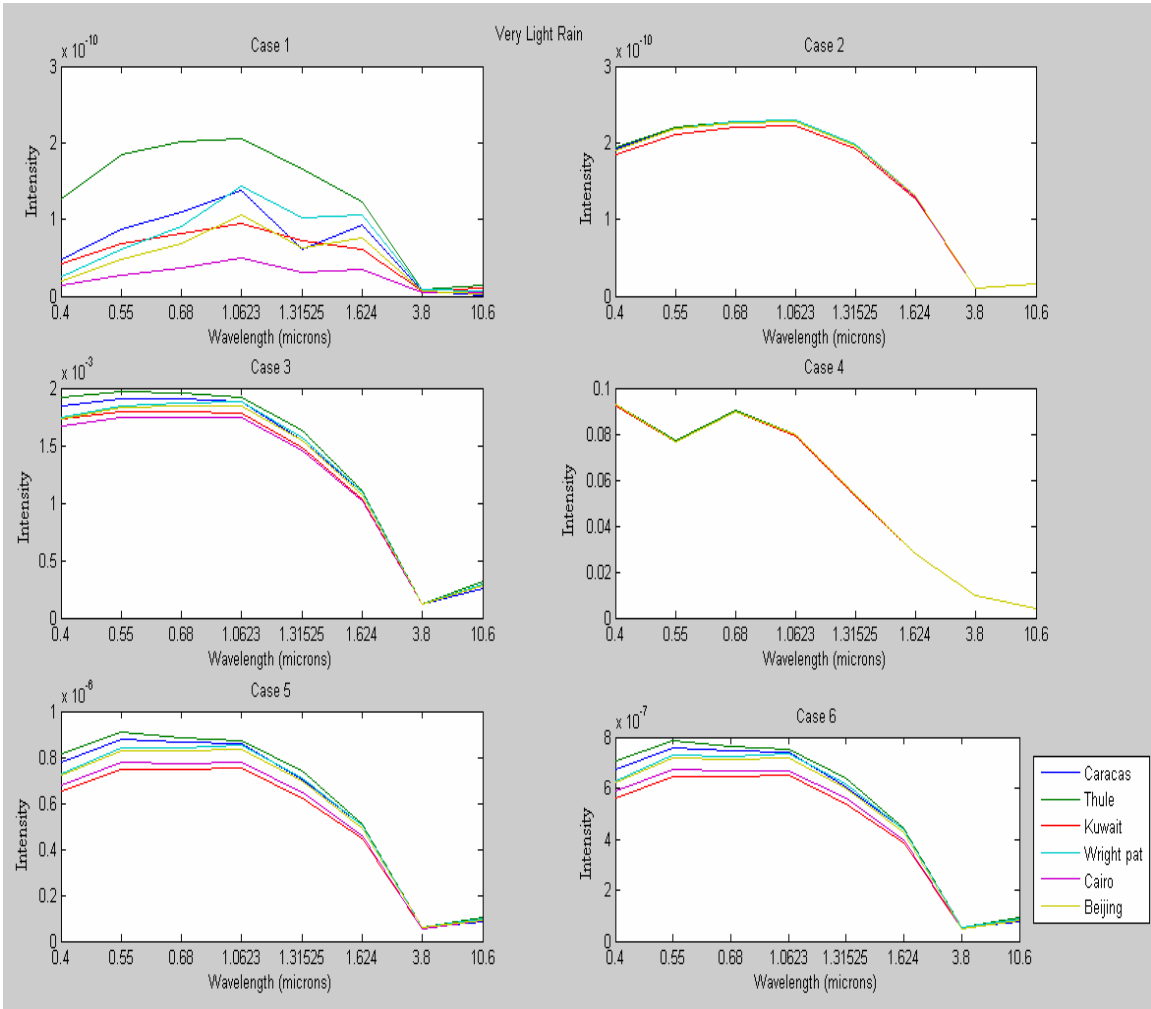


Figure 19: Very Light Rain

Table 14: Light Rain

Atmosphere Type	Aerosol Type	Site id	Percentile	Time of Day	Use Clouds	Cloud Type	Cloud Upper Altitude	Cloud Lower Altitude
16	0	265	5	9	1	8	1,0001	0
16	0	16	5	9	1	8	1,0001	0
16	0	95	5	9	1	8	1,0001	0
16	0	253	5	9	1	8	1,0001	0
16	0	157	5	9	1	8	1,0001	0
16	0	145	5	9	1	8	1,0001	0

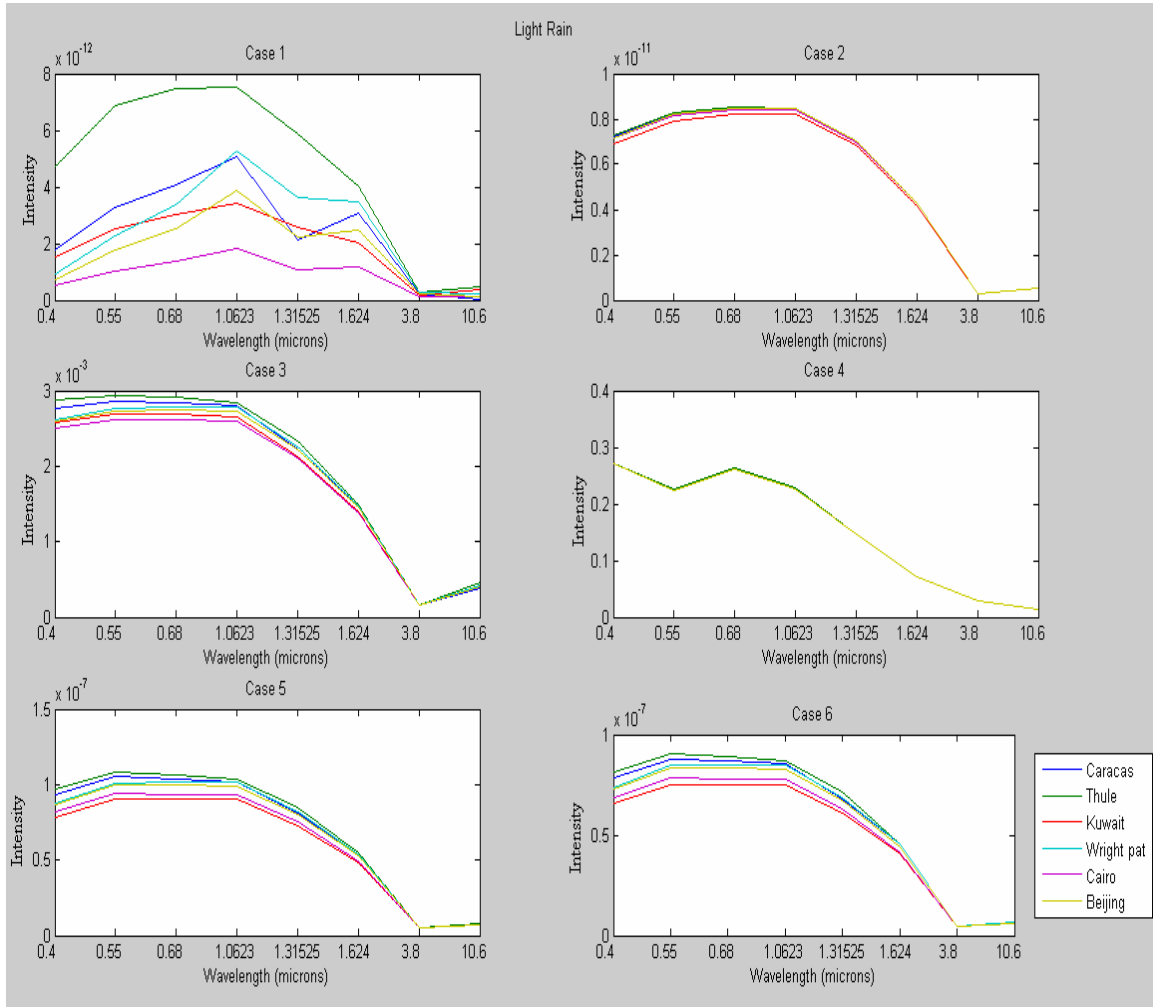


Figure 20: Light Rain

Table 15: Moderate Rain

Atmosphere Type	Aerosol Type	Site id	Percentile	Time of Day	Use Clouds	Cloud Type	Cloud Upper Altitude	Cloud Lower Altitude
16	0	265	5	9	1	9	1,0001	0
16	0	16	5	9	1	9	1,0001	0
16	0	95	5	9	1	9	1,0001	0
16	0	253	5	9	1	9	1,0001	0
16	0	157	5	9	1	9	1,0001	0
16	0	145	5	9	1	9	1,0001	0

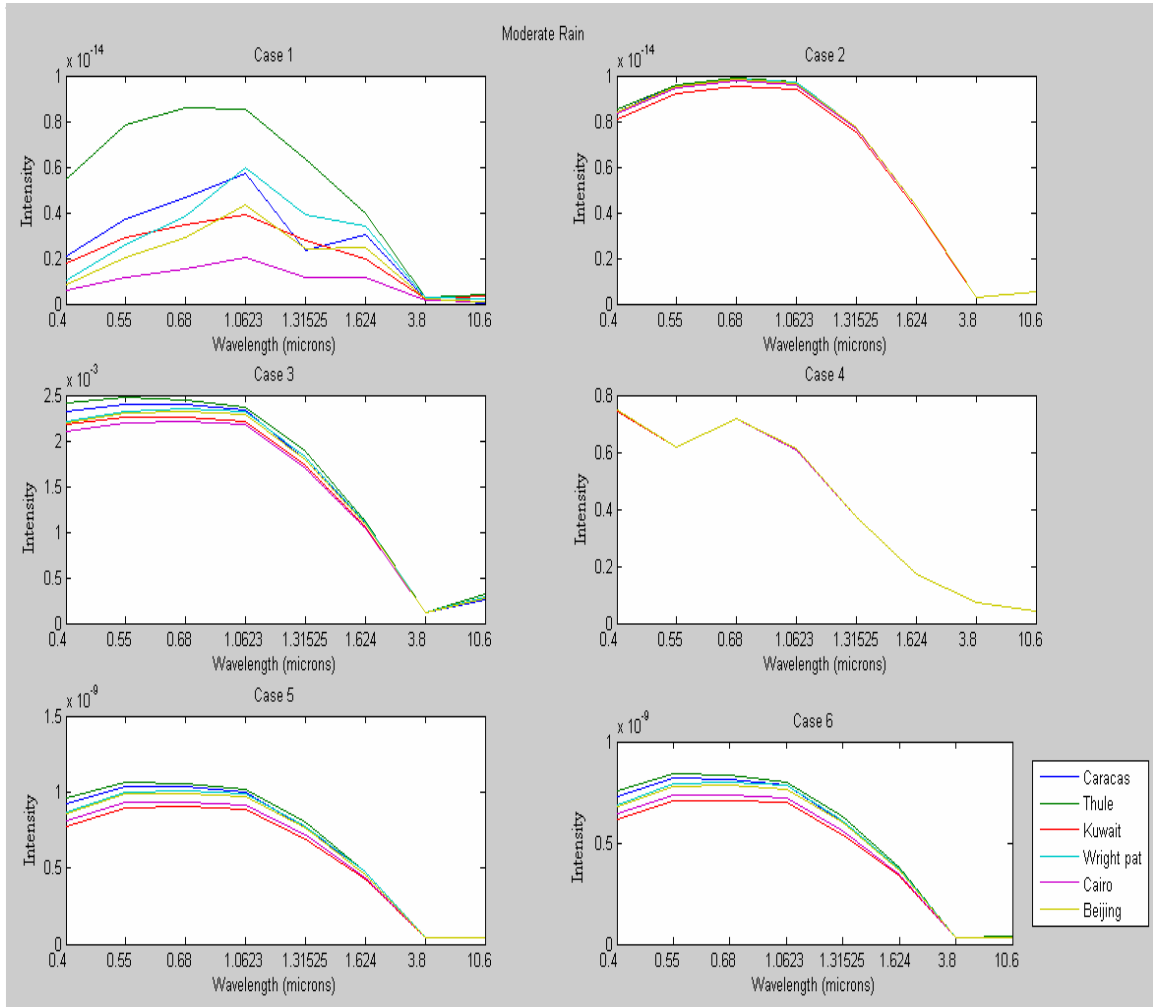


Figure 21: Moderate Rain

Table 16: Heavy Rain

Atmosphere Type	Aerosol Type	Site id	Percentile	Time of Day	Use Clouds	Cloud Type	Cloud Upper Altitude	Cloud Lower Altitude
16	0	265	5	9	1	10	1,0001	0
16	0	16	5	9	1	10	1,0001	0
16	0	95	5	9	1	10	1,0001	0
16	0	253	5	9	1	10	1,0001	0
16	0	157	5	9	1	10	1,0001	0
16	0	145	5	9	1	10	1,0001	0

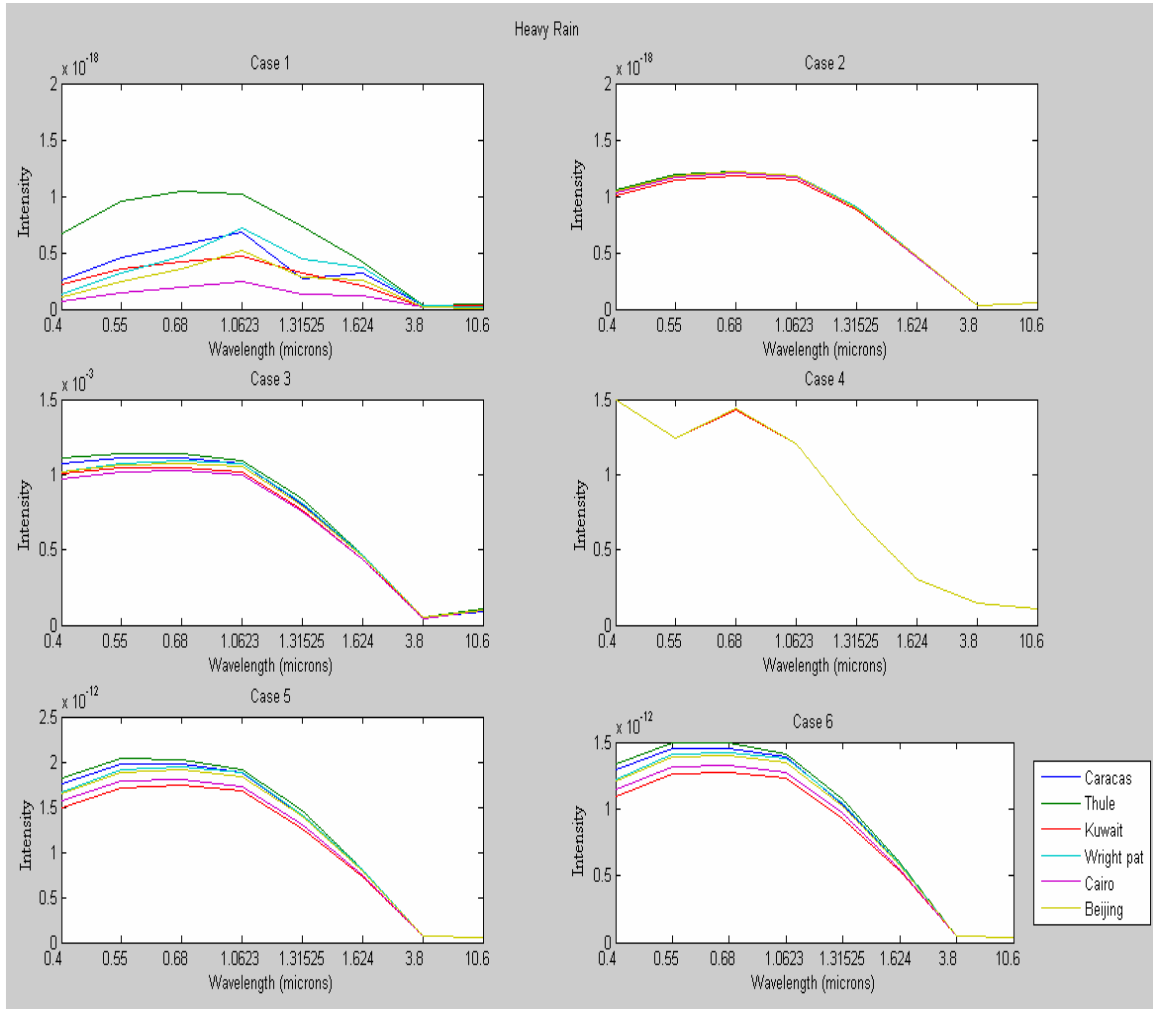


Figure 22: Heavy Rain

Table 17: Extreme Rain

Atmosphere Type	Aerosol Type	Site id	Percentile	Time of Day	Use Clouds	Cloud Type	Cloud Upper Altitude	Cloud Lower Altitude
16	0	265	5	9	1	11	1,0001	0
16	0	16	5	9	1	11	1,0001	0
16	0	95	5	9	1	11	1,0001	0
16	0	253	5	9	1	11	1,0001	0
16	0	157	5	9	1	11	1,0001	0
16	0	145	5	9	1	11	1,0001	0

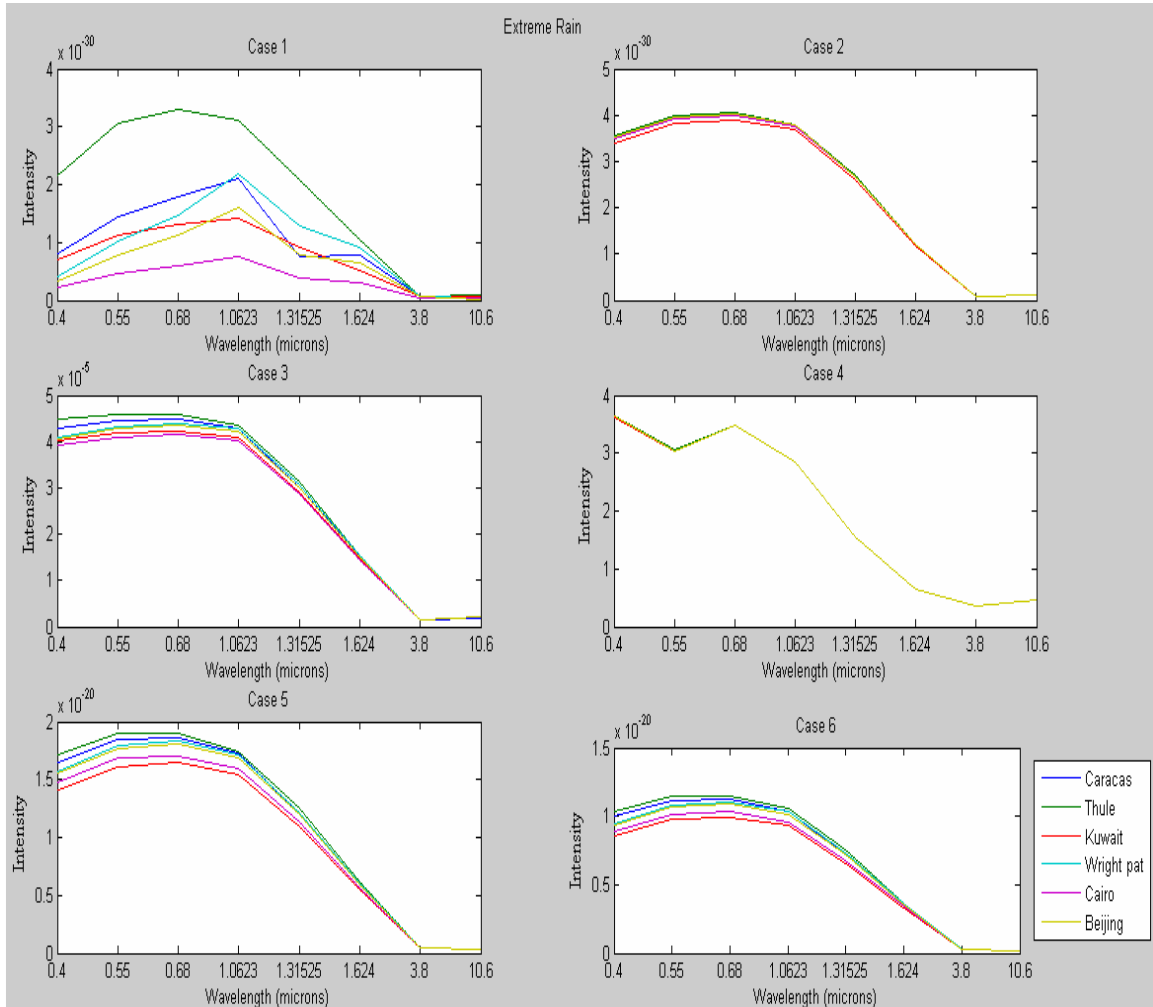


Figure 23: Extreme Rain

Table 18: Relative Humidity 1st Percentile

Atmosphere Type	Aerosol Type	Site id	Percentile	Time of Day	Use Clouds	Cloud Type	Cloud Upper Altitude	Cloud Lower Altitude
16	0	265	1	9	0	0	0	0
16	0	16	1	9	0	0	0	0
16	0	95	1	9	0	0	0	0
16	0	253	1	9	0	0	0	0
16	0	157	1	9	0	0	0	0
16	0	145	1	9	0	0	0	0

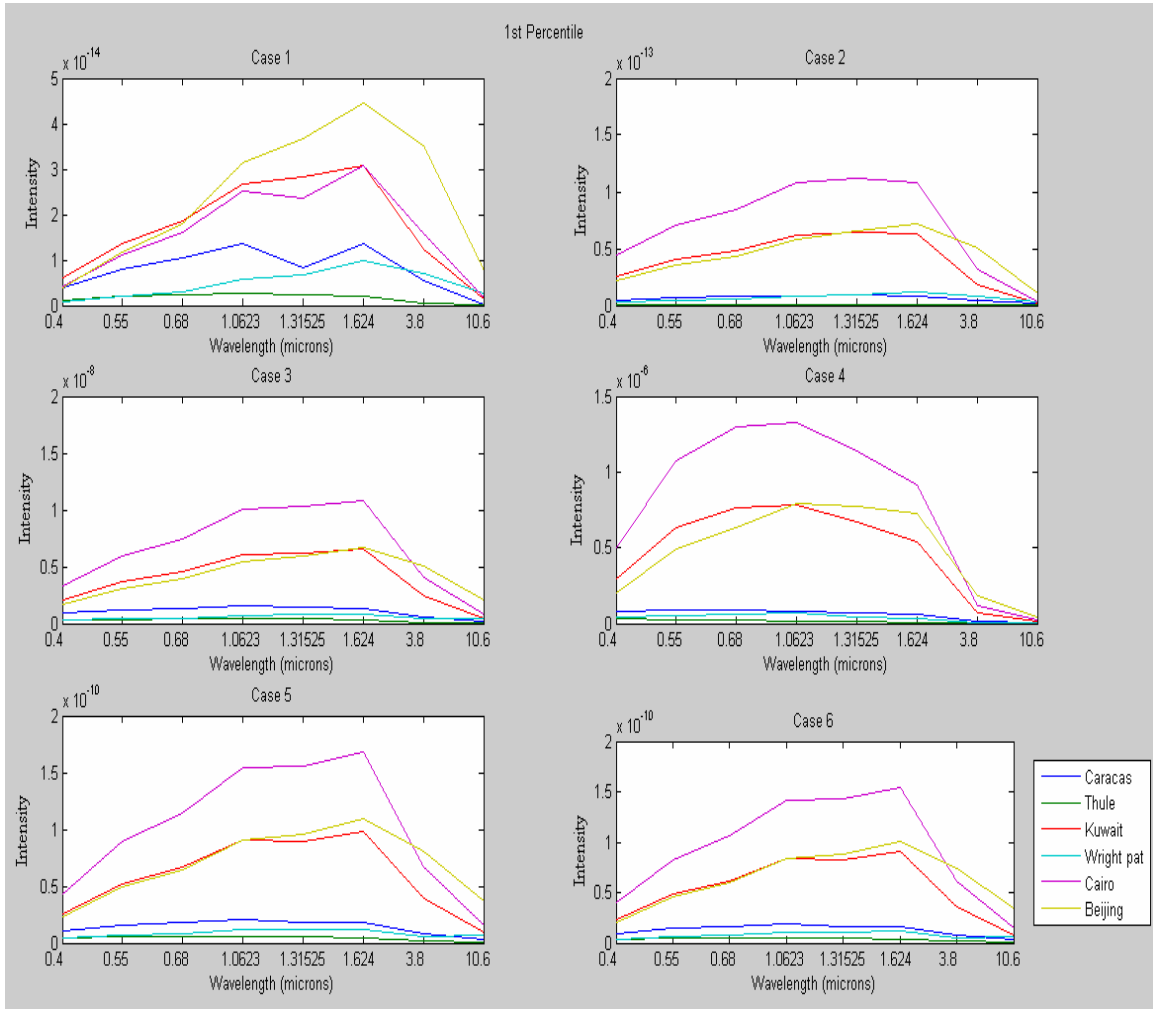


Figure 24: Relative Humidity 1st Percentile

Table 19: Relative Humidity 50th Percentile

Atmosphere Type	Aerosol Type	Site id	Percentile	Time of Day	Use Clouds	Cloud Type	Cloud Upper Altitude	Cloud Lower Altitude
16	0	265	5	9	0	0	0	0
16	0	16	5	9	0	0	0	0
16	0	95	5	9	0	0	0	0
16	0	253	5	9	0	0	0	0
16	0	157	5	9	0	0	0	0
16	0	145	5	9	0	0	0	0

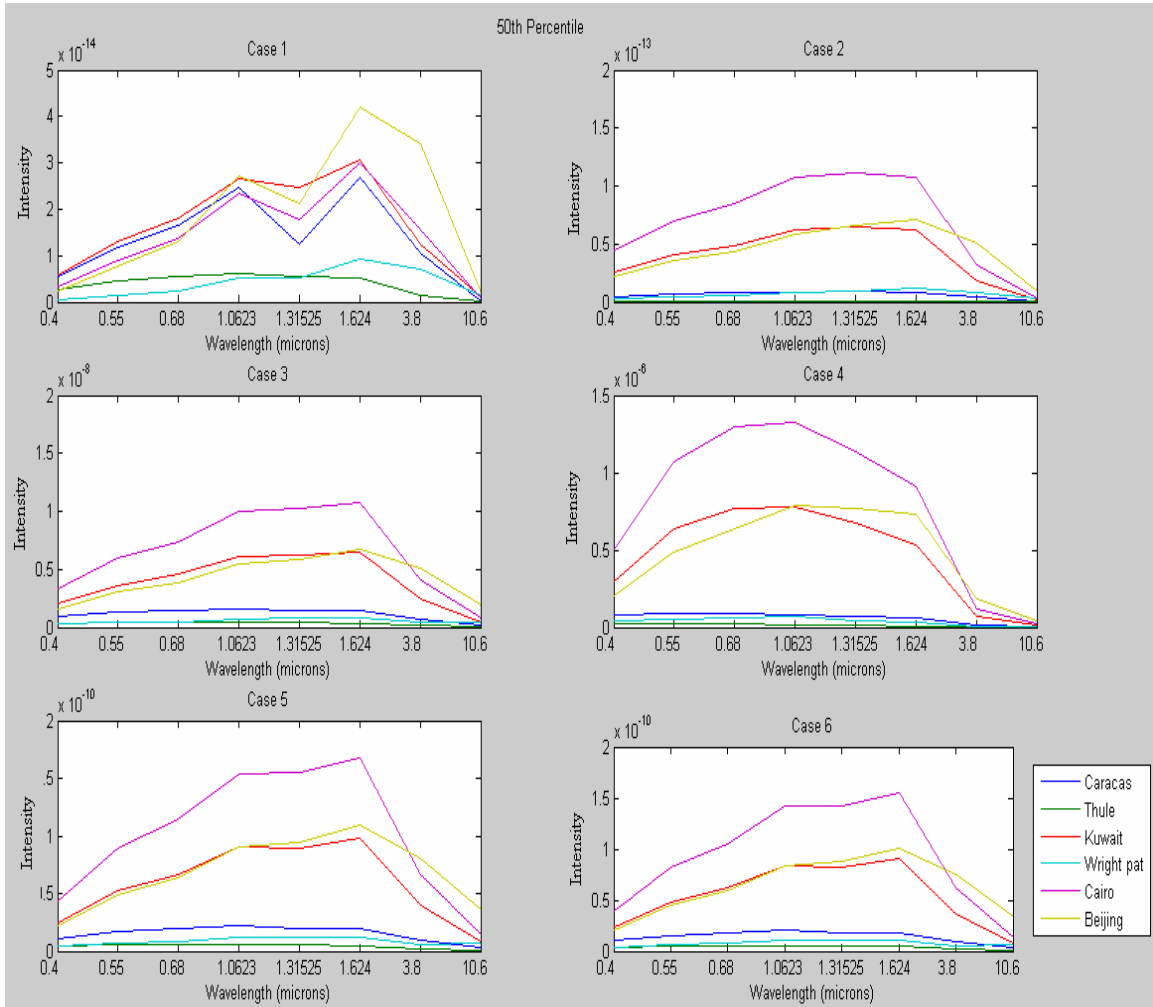


Figure 25: Relative Humidity 50th Percentile

Table 20: Relative Humidity 99th Percentile

Atmosphere Type	Aerosol Type	Site id	Percentile	Time of Day	Use Clouds	Cloud Type	Cloud Upper Altitude	Cloud Lower Altitude
16	0	265	9	9	0	0	0	0
16	0	16	9	9	0	0	0	0
16	0	95	9	9	0	0	0	0
16	0	253	9	9	0	0	0	0
16	0	157	9	9	0	0	0	0
16	0	145	9	9	0	0	0	0

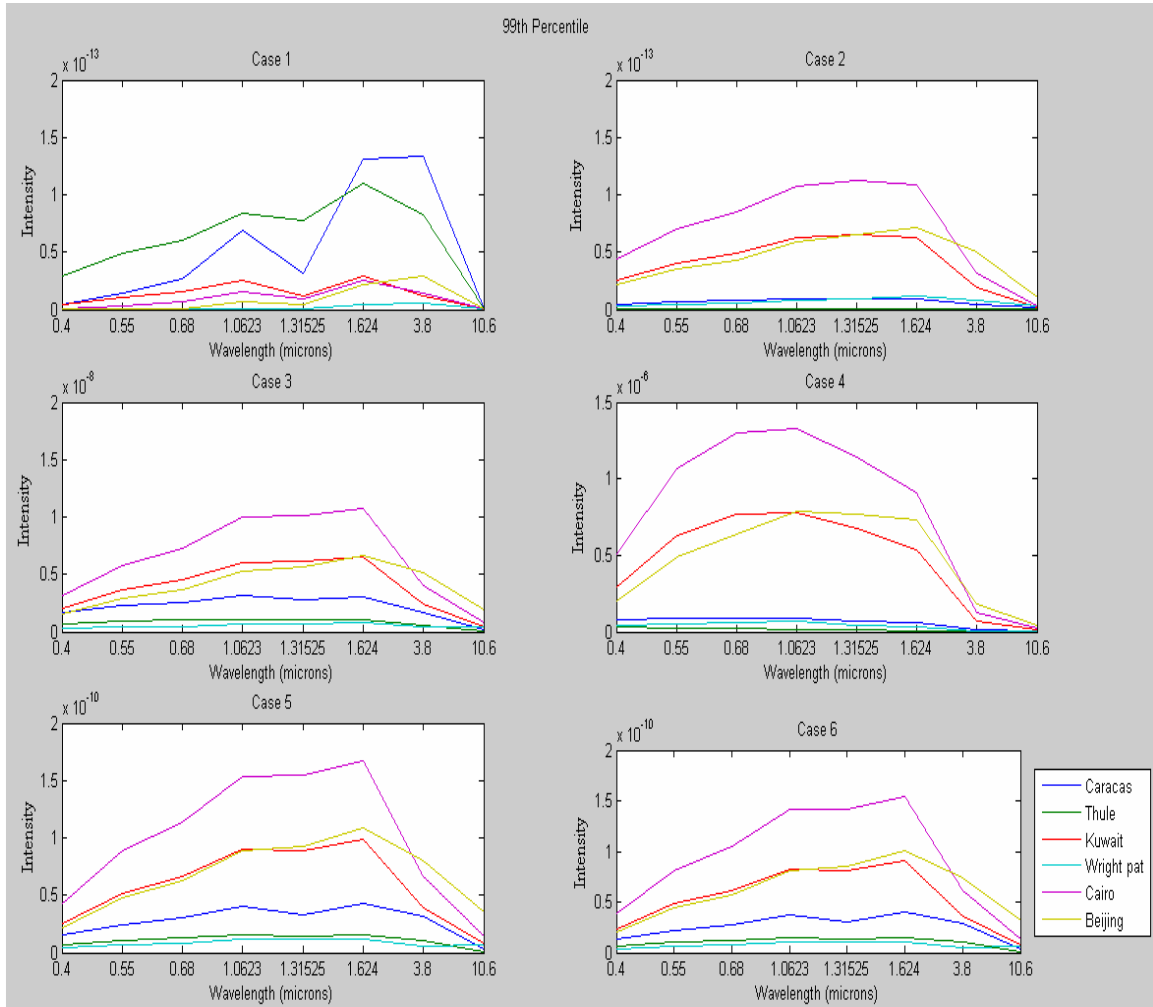


Figure 26: Relative Humidity 99th Percentile

Table 21: Time of Day 0000-0300

Atmosphere Type	Aerosol Type	Site id	Percentile	Time of Day	Use Clouds	Cloud Type	Cloud Upper Altitude	Cloud Lower Altitude
16	0	265	5	1	0	0	0	0
16	0	16	5	1	0	0	0	0
16	0	95	5	1	0	0	0	0
16	0	253	5	1	0	0	0	0
16	0	157	5	1	0	0	0	0
16	0	145	5	1	0	0	0	0

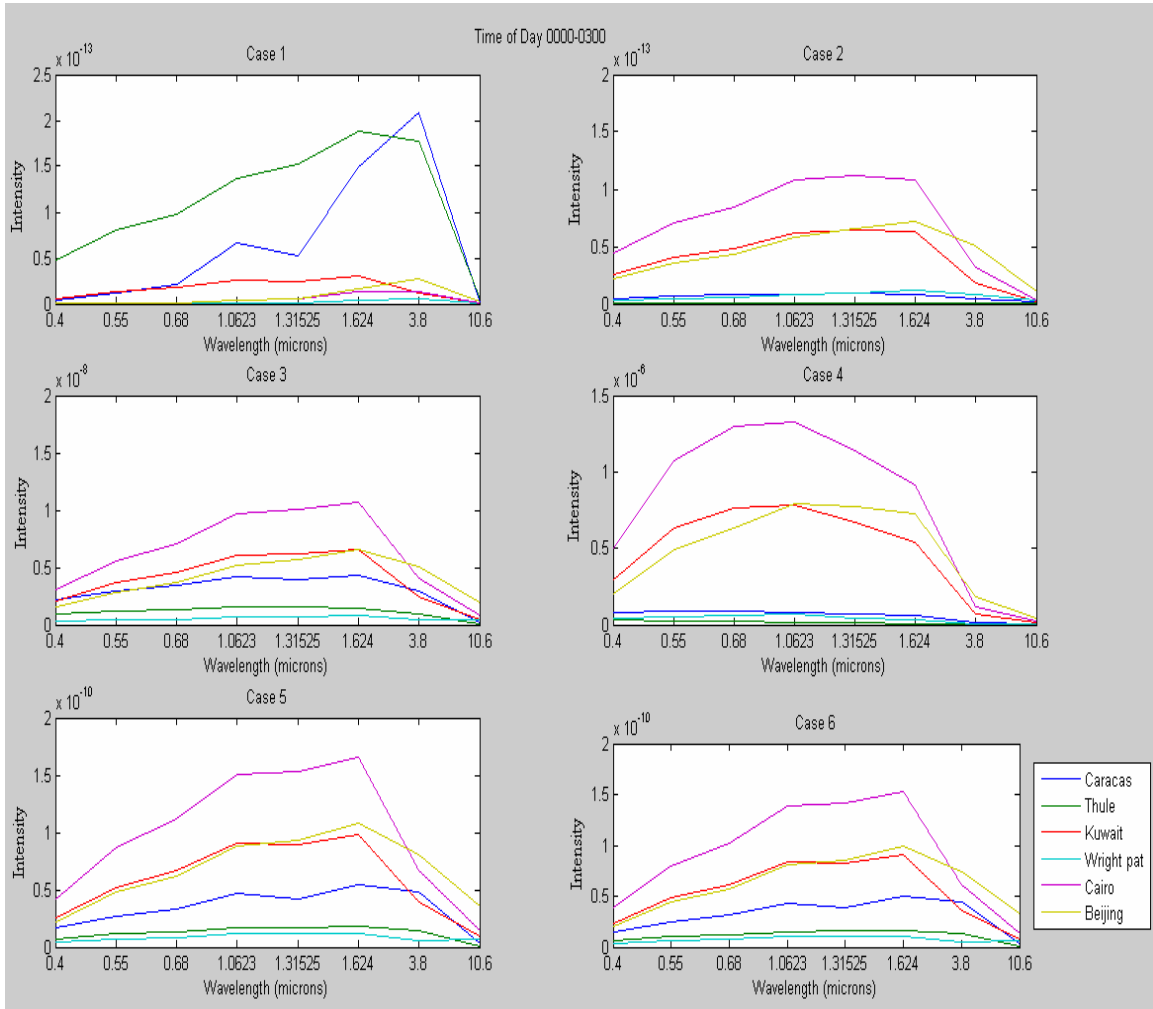


Figure 27: Time of Day 0000-0300

Table 22: Time of Day 0600-0900

Atmosphere Type	Aerosol Type	Site id	Percentile	Time of Day	Use Clouds	Cloud Type	Cloud Upper Altitude	Cloud Lower Altitude
16	0	265	5	3	0	0	0	0
16	0	16	5	3	0	0	0	0
16	0	95	5	3	0	0	0	0
16	0	253	5	3	0	0	0	0
16	0	157	5	3	0	0	0	0
16	0	145	5	3	0	0	0	0

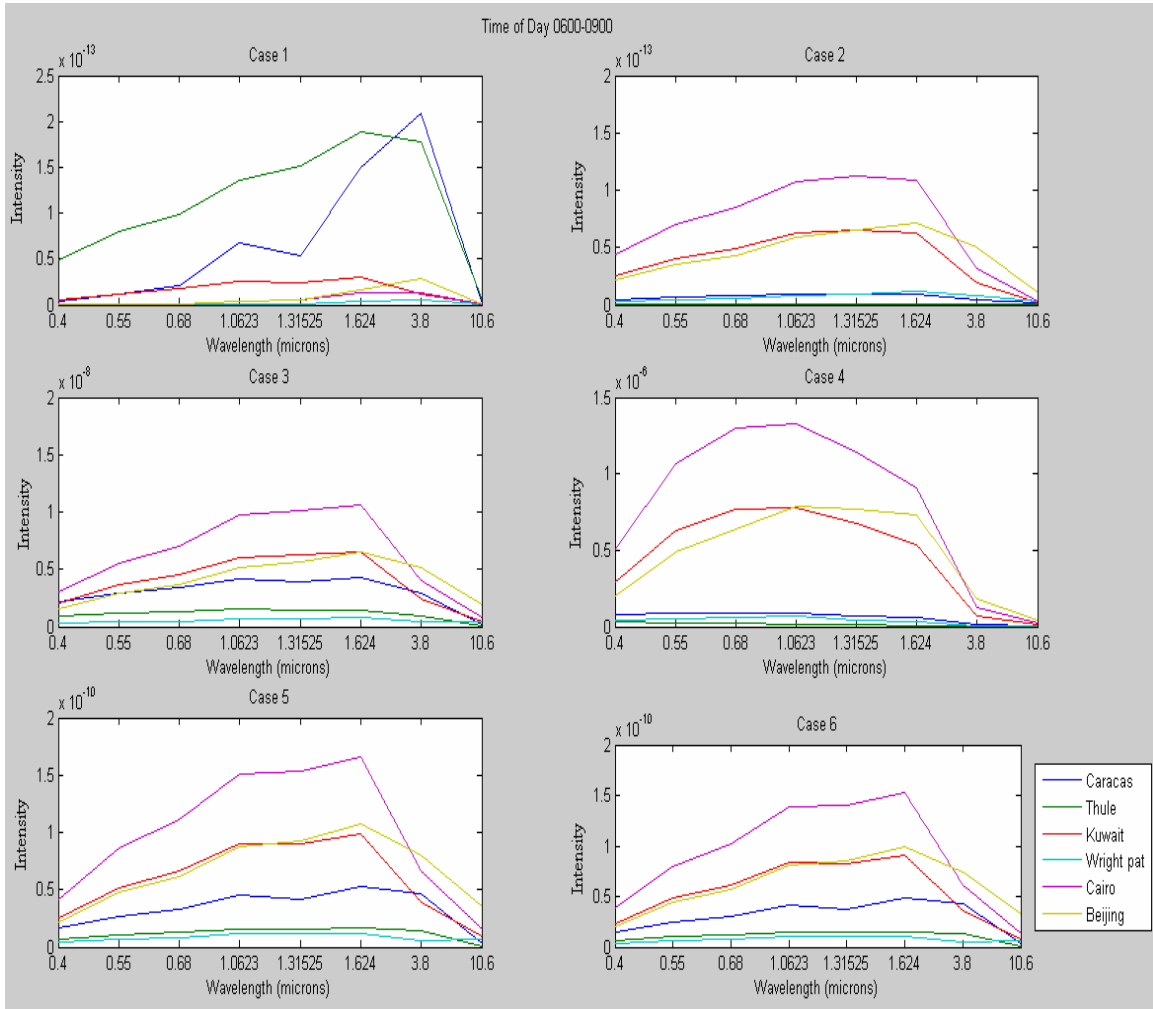


Figure 28: Time of Day 0600-0900

Table 23: Time of Day 1200-1500

Atmosphere Type	Aerosol Type	Site id	Percentile	Time of Day	Use Clouds	Cloud Type	Cloud Upper Altitude	Cloud Lower Altitude
16	0	265	5	5	0	0	0	0
16	0	16	5	5	0	0	0	0
16	0	95	5	5	0	0	0	0
16	0	253	5	5	0	0	0	0
16	0	157	5	5	0	0	0	0
16	0	145	5	5	0	0	0	0

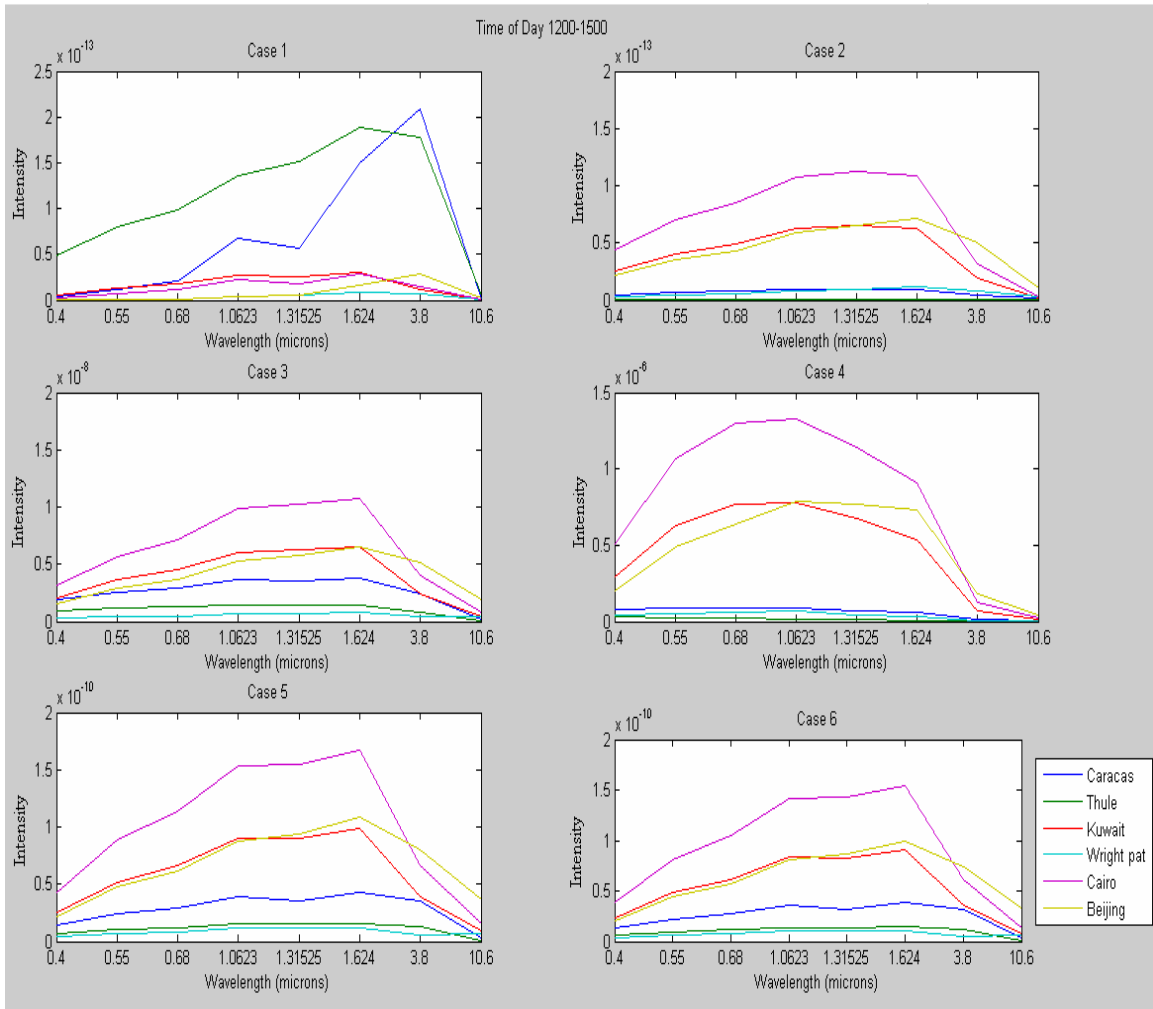


Figure 29: Time of Day 1200-1500

Appendix B

Table 24: Maximum Permissible Exposure (MPE) for small source ocular exposure to a laser beam (ANSI Z136.1, 2000)

Wavelength (μm)	Exposure Duration, t (s)	MPE		Notes
		($\text{J} \cdot \text{cm}^{-2}$)	($\text{W} \cdot \text{cm}^{-2}$)	
Ultraviolet				
0.180 to 0.302	10^{-9} to 3×10^4	3×10^{-3}		or $0.56 t^{0.25}$ whichever is lower. (See Tables 8 and 9 for limiting apertures)
0.303	10^{-9} to 3×10^4	4×10^{-3}		
0.304	10^{-9} to 3×10^4	6×10^{-3}		
0.305	10^{-9} to 3×10^4	10×10^{-3}		
0.306	10^{-9} to 3×10^4	16×10^{-3}		
0.307	10^{-9} to 3×10^4	25×10^{-3}		
0.308	10^{-9} to 3×10^4	40×10^{-3}		
0.309	10^{-9} to 3×10^4	63×10^{-3}		
0.310	10^{-9} to 3×10^4	0.1		
0.311	10^{-9} to 3×10^4	0.16		
0.312	10^{-9} to 3×10^4	0.25		
0.313	10^{-9} to 3×10^4	0.40		
0.314	10^{-9} to 3×10^4	0.63		
0.315 to 0.400	10^{-9} to 10	$0.56 t^{0.25}$		
0.315 to 0.400	10 to 3×10^4	1.0		
Visible and Near Infrared				
0.400 to 0.700	10^{-13} to 10^{-11}	1.5×10^{-8}		(See Tables 8 and 9 for limiting apertures) For multiple pulses apply correction factor C_p given in Table 6.
0.400 to 0.700	10^{-11} to 10^{-9}	$2.7 t^{0.75}$		
0.400 to 0.700	10^{-9} to 18×10^{-6}	5.0×10^{-7}		
0.400 to 0.700	18×10^{-6} to 10	$1.8 t^{0.75} \times 10^{-3}$		
0.400 to 0.450	10 to 100	1×10^{-2}		
0.450 to 0.500	10 to T_1		1×10^{-3}	
0.450 to 0.500	T_1 to 100	$C_B \times 10^{-2}$		
0.400 to 0.500	100 to 3×10^4		$C_B \times 10^{-4}$	
0.500 to 0.700	10 to 3×10^4		1×10^{-3}	
0.700 to 1.050	10^{-13} to 10^{-11}	$1.5 C_A \times 10^{-8}$		
0.700 to 1.050	10^{-11} to 10^{-9}	$2.7 C_A t^{0.75}$		
0.700 to 1.050	10^{-9} to 18×10^{-6}	$5.0 C_A \times 10^{-7}$		
0.700 to 1.050	18×10^{-6} to 10	$1.8 C_A t^{0.75} \times 10^{-3}$		
0.700 to 1.050	10 to 3×10^4		$C_A \times 10^{-3}$	
1.050 to 1.400	10^{-13} to 10^{-11}	$1.5 C_C \times 10^{-7}$		
1.050 to 1.400	10^{-11} to 10^{-9}	$27.0 C_C t^{0.75}$		
1.050 to 1.400	10^{-9} to 50×10^{-6}	$5.0 C_C \times 10^{-6}$		
1.050 to 1.400	50×10^{-6} to 10	$9.0 C_C t^{0.75} \times 10^{-3}$		
1.050 to 1.400	10 to 3×10^4		$5.0 C_C \times 10^{-3}$	
Far Infrared				
1.400 to 1.500	10^{-9} to 10^{-3}	0.1		For multiple pulses apply correction factor C_p given in Table 6 (See Tables 8 and 9 for limiting apertures)
1.400 to 1.500	10^{-3} to 10	$0.56 t^{0.25}$		
1.400 to 1.500	10 to 3×10^4		0.1	
1.500 to 1.800	10^{-9} to 10	1.0		
1.500 to 1.800	10 to 3×10^4		0.1	
1.800 to 2.600	10^{-9} to 10^{-3}	0.1		
1.800 to 2.600	10^{-3} to 10	$0.56 t^{0.25}$		
1.800 to 2.600	10 to 3×10^4		0.1	
2.600 to 10^3	10^{-9} to 10^{-7}	1×10^{-2}		
2.600 to 10^3	10^{-7} to 10	$0.56 t^{0.25}$		
2.600 to 10^3	10 to 3×10^4		0.1	

¹ See Table 6 and Figures 8 and 9 for correction factors C_B , C_C and time T_1 . For exposure durations greater than 10 seconds and extended sources in the retinal hazard region (0.400 to 1.4 μm), see Table 5b.

- Notes:
1. For repeated (pulsed) exposures, see Section 8.2.3.
 2. The wavelength region λ_1 to λ_2 means $\lambda_1 \leq \lambda < \lambda_2$, e.g., 0.180 to 0.302 μm means $0.180 \leq \lambda < 0.302 \mu\text{m}$.
 3. Dual Limit Application: In the Dual Limit Wavelength Region (0.400 to 0.600 μm), the listed MPE is the lower value of the photochemical and thermal MPEs as determined by T_1 .

Table 25: Maximum Permissible Exposure (MPE) for extended-source ocular exposure to a laser beam for long exposure durations (ANSI Z136.1, 2000)

Wavelength (μm)	Exposure Duration, t (s)	MPE		Notes
		($\text{J} \cdot \text{cm}^{-2}$) except as noted	($\text{W} \cdot \text{cm}^{-2}$) except as noted	
Visible				
0.400 to 0.700	10^{-13} to 10^{-11}	$1.5 C_E \times 10^{-8}$		(See Tables 8 and 9 for limiting apertures)
0.400 to 0.700	10^{-11} to 10^{-9}	$2.7 C_E t^{0.75}$		
0.400 to 0.700	10^{-9} to 18×10^{-6}	$5.0 C_E \times 10^{-7}$		
0.400 to 0.700	18×10^{-6} to 0.7	$1.8 C_E t^{0.75} \times 10^{-3}$		
Photochemical				
<i>Dual Limits for 400 - 600 nm visible laser exposure for $t > 0.7$ s</i>				
For $\alpha \leq 11$ mrad, the MPE is expressed as irradiance and radiant exposure*				
0.400 to 0.600	0.7 to 100	$C_B \times 10^{-2}$		(See Tables 8 and 9 for limiting apertures)
0.400 to 0.600	100 to 3×10^4		$C_B \times 10^{-4}$	
For $\alpha > 11$ mrad, the MPE is expressed as radiance and integrated radiance*				
0.400 to 0.600	0.7 to 1×10^4	$100 C_B \text{ J} \cdot \text{cm}^{-2} \cdot \text{sr}^{-1}$		(See Table 8 for limiting cone angle γ)
0.400 to 0.600	1×10^4 to 3×10^4		$C_B \times 10^{-2} \text{ W} \cdot \text{cm}^{-2} \cdot \text{sr}^{-1}$	
<i>and</i>				
Thermal				
0.400 to 0.700	0.7 to T_2	$1.8 C_E t^{0.75} \times 10^{-3}$		
0.400 to 0.700	T_2 to 3×10^4		$1.8 C_E T_2^{-0.25} \times 10^{-3}$	
Near Infrared				
0.700 to 1.050	10^{-13} to 10^{-11}	$1.5 C_A C_E \times 10^{-8}$		(See Tables 8 and 9 for limiting apertures)
0.700 to 1.050	10^{-11} to 10^{-9}	$2.7 C_A C_E t^{0.75}$		
0.700 to 1.050	10^{-9} to 18×10^{-6}	$5.0 C_A C_E \times 10^{-7}$		
0.700 to 1.050	18×10^{-6} to T_2	$1.8 C_A C_E t^{0.75} \times 10^{-3}$		
0.700 to 1.050	T_2 to 3×10^4		$1.8 C_A C_E T_2^{-0.25} \times 10^{-3}$	
1.050 to 1.400	10^{-13} to 10^{-11}	$1.5 C_C C_E \times 10^{-7}$		
1.050 to 1.400	10^{-11} to 10^{-9}	$27.0 C_C C_E t^{0.75}$		
1.050 to 1.400	10^{-9} to 50×10^{-6}	$5.0 C_C C_E \times 10^{-6}$		
1.050 to 1.400	50×10^{-6} to T_2	$9.0 C_C C_E t^{0.75} \times 10^{-3}$		
1.050 to 1.400	T_2 to 3×10^4		$9.0 C_C C_E T_2^{-0.25} \times 10^{-3}$	

¹See Table 6 and Figures 8, 9 and 11 for correction factors C_A, C_B, C_C, C_E, C_F , and time T_2 .

*For sources subtending an angle greater than 11 mrad, the limit may also be expressed as an integrated radiance $L_p = 100 C_B \text{ J} \cdot \text{cm}^{-2} \cdot \text{sr}^{-1}$ for $0.7 \text{ s} \leq t < 10^4 \text{ s}$ and $L_e = C_B \times 10^{-2} \text{ W} \cdot \text{cm}^{-2} \cdot \text{sr}^{-1}$ for $t \geq 10^4 \text{ s}$ as measured through a limiting cone angle γ . These correspond to values of $\text{J} \cdot \text{cm}^{-2}$ for $10 \text{ s} \leq t < 100 \text{ s}$ and $\text{W} \cdot \text{cm}^{-2}$ for $t \geq 100 \text{ s}$ as measured through a limiting cone angle γ .

$\gamma = 11$ mrad for $0.7 \text{ s} \leq t < 100 \text{ s}$,

$\gamma = 1.1 \times t^{0.5}$ mrad for $100 \text{ s} \leq t < 10^4 \text{ s}$

$\gamma = 110$ mrad for $10^4 \text{ s} \leq t < 3 \times 10^4 \text{ s}$

See Figure 3 for γ and Appendix B7.2 for examples.

Notes: 1. For repeated (pulsed) exposures, see Section 8.2.3.
2. The wavelength region λ_1 to λ_2 means $\lambda_1 \leq \lambda < \lambda_2$, e.g., 1.180 to 1.302 μm means $1.180 \leq \lambda < 1.302 \mu\text{m}$.
3. Dual Limit Application: In the Dual Limit wavelength region (0.400 to 0.600 μm), the exposure limit is the lower value of the determined photochemical and thermal exposure limit.

Table 26: Maximum Permissible Exposure (MPE) for skin exposure to a laser beam (ANSI Z136.1, 2000)

Wavelength (μm)	Exposure Duration, t (s)	MPE		Notes
		($\text{J} \cdot \text{cm}^{-2}$)	($\text{W} \cdot \text{cm}^{-2}$)	
Ultraviolet				
0.180 to 0.302	10^{-9} to 3×10^4	3×10^{-3}		} or $0.56 t^{0.25}$ whichever is lower. 3.5 mm limiting aperture: (See Table 8)
0.303	10^{-9} to 3×10^4	4×10^{-3}		
0.304	10^{-9} to 3×10^4	6×10^{-3}		
0.305	10^{-9} to 3×10^4	1.0×10^{-2}		
0.306	10^{-9} to 3×10^4	1.6×10^{-2}		
0.307	10^{-9} to 3×10^4	25×10^{-3}		
0.308	10^{-9} to 3×10^4	40×10^{-3}		
0.309	10^{-9} to 3×10^4	63×10^{-3}		
0.310	10^{-9} to 3×10^4	0.1		
0.311	10^{-9} to 3×10^4	0.16		
0.312	10^{-9} to 3×10^4	0.25		
0.313	10^{-9} to 3×10^4	0.40		
0.314	10^{-9} to 3×10^4	0.63		
0.315 to 0.400	10^{-9} to 10	$0.56 t^{0.25}$		
0.315 to 0.400	10 to 10^3	1		
0.315 to 0.400	10^3 to 3×10^4		1×10^{-3}	
Visible and Near Infrared				
0.400 to 1.400	10^{-9} to 10^{-7}	$2 C_A \times 10^{-2}$		} 3.5 mm limiting aperture: (See Table 8)
	10^{-7} to 10	$1.1 C_A t^{0.25}$		
	10 to 3×10^4		$0.2 C_A$	
Far Infrared				
1.400 to 1.500	10^{-9} to 10^{-3}	0.1		} (See Table 8 for limiting apertures)
1.400 to 1.500	10^{-3} to 10	$0.56 t^{0.25}$		
1.400 to 1.500	10 to 3×10^4		0.1	
1.500 to 1.800	10^{-9} to 10	1.0		
1.500 to 1.800	10 to 3×10^4		0.1	
1.800 to 2.600	10^{-9} to 10^{-3}	0.1		
1.800 to 2.600	10^{-3} to 10	$0.56 t^{0.25}$		
1.800 to 2.600	10 to 3×10^4		0.1	
2.600 to 10^3	10^{-9} to 10^{-7}	1×10^{-2}		
2.600 to 10^3	10^{-7} to 10	$0.56 t^{0.25}$		
2.600 to 10^3	10 to 3×10^4		0.1	

* See 8.4.2 for large beam cross-sections and Table 6 for correction factor C_A .

NOTE: The wavelength region λ_1 to λ_2 means $\lambda_1 \leq \lambda < \lambda_2$, e.g., 0.315 to 0.400 μm means $0.314 \leq \lambda < 0.400 \mu\text{m}$.

Table 27: Parameters and Correction Factors (ANSI Z136.1, 2000)

Parameters/Correction Factors	Wavelength (μm)	Figure*
$T_1 = 10 \times 10^{20(\lambda - 0.450)}$ **	0.450 to 0.500	9a
$T_2 = 10 \times 10^{(\alpha - 1.5)/98.5}$ ***	0.400 to 1.400	9b
$C_B = 1.0$	0.400 to 0.450	8c
$C_B = 10^{20(\lambda - 0.450)}$	0.450 to 0.600	8c
$C_A = 1.0$	0.400 to 0.700	8a
$C_A = 10^{2(\lambda - 0.700)}$	0.700 to 1.050	8a
$C_A = 5.0$	1.050 to 1.400	8a
$C_P = \pi^{-0.25}$ ****	0.180 to 1000	13
$C_E = 1.0 \quad \alpha < \alpha_{\min}$	0.400 to 1.400	—
$C_E = \alpha / \alpha_{\min} \quad \alpha_{\min} \leq \alpha \leq \alpha_{\max}$	0.400 to 1.400	—
$C_E = \alpha^2 / (\alpha_{\max} \alpha_{\min}) \quad \alpha > \alpha_{\max}$	0.400 to 1.400	—
$C_C = 1.0$	1.050 to 1.150	8b
$C_C = 10^{18(\lambda - 1.150)}$	1.150 to 1.200	8b
$C_C = 8$	1.200 to 1.400	8b

* See figures for graphic representation.

** $T_1 = 10$ s for $\lambda = 0.450 \mu\text{m}$, and $T_1 = 100$ s for $\lambda = 0.500 \mu\text{m}$.

*** $T_2 = 10$ s for $\alpha < 1.5$ mrad, and $T_2 = 100$ s for $\alpha > 100$ mrad.

**** See Section 8.2.3 for discussion of C_p and Section 8.2.3.2 for discussion of pulse repetition frequencies below 55 kHz (0.4 to 1.05 μm) and below 20 kHz (1.05 to 1.4 μm).

Notes:

- For wavelengths between 0.400 and 1.400 μm :
 $\alpha_{\min} = 1.5$ mrad $\alpha_{\max} = 100$ mrad

- Wavelengths must be expressed in micrometers and angles in milliradians for calculations.

The wavelength region λ_1 to λ_2 means $\lambda_1 \leq \lambda < \lambda_2$,
e.g., 0.550 to 0.700 μm means $0.550 \leq \lambda < 0.700 \mu\text{m}$.

Bibliography

1. About Inventors. *Laser History*. 2005 About.com
<http://inventors.about.com/library/inventors/bllaser.htm>.
2. Air Force Technology. *ABL YAL IA Airborne Laser*. 2005 airforce-technology.com <http://www.airforce-technology.com/projects/abl/>.
3. American National Standards Institute. *American National Standard for the Safe Use of Lasers/ Secretariat, the Laser Institute of America* [New York]: American National Standards Institute; Orlando, FL: Laser Institute of America, c2000.
4. Bartell, R.J. *Application of the HELEEOS HEL Scaling Law Model to LASINT Scenarios* Air Force Institute of Technology and Riverside Research Institute, 2004.
5. Deering, Michael F. *The Limit of Human Vision* Sun Microsystems 1994.
6. "Descriptions [of ACTDs]." Excerpt from unpublished article. n. page.
<http://www.acq.osd.mil/actd/descript.htm>. 17 Dec 2002.
7. eScience. *The Human Eye: Main Characteristics of the Sight* 2006
<http://escience.anu.edu.au/lecture/ivr/sight/eyeMainCharacteristics2.en.html>.
8. Fiorino, S. T. The HELEEOS Atmospheric Effects Package: A Probabilistic Method for Evaluating: Uncertainty in Low-Altitude High Energy Laser Effectiveness. Air Force Institute of Technology, Center for Directed Energy, 2004.
9. Fiorino, Steven T. Class handout, METG 611, Space Effects on EM Propagation. Department of Physics, Air Force Institute of Technology, Wright-Patterson AFB OH, Jan 2005.
10. Global Security. *Advanced Tactical Laser*. 2005
<http://www.globalsecurity.org/military/systems/aircraft/systems/atl.htm>.
11. "Introduction to ACTDs." Excerpt from unpublished article.
<http://www.acq.osd.mil/actd/intro.htm>. 17 December 2002.
12. Kyle, Thomas G. *Atmospheric Transmission, Emission, and Scattering*. Oxford; New York: Pergamon Press, 1991.
13. Laser Weapon Systems. Lecture Slides, LWS Short Course. Center for Directed Energy, Air Force Institute of Technology, Wright-Patterson AFB OH, Jan 2005.

14. Mallow, Alex and Leon Chabot. *Laser Safety Handbook*. New York: Van Nostrand Reinhold Company, 1978.
15. MDA Link. *Making Ballistic Missile Defense a Reality...* 2005 Missile Defense Agency <http://www.mda.mil/mdalink/html/mdalink.html>.
16. Petty, Grant W. *A First Course in Atmospheric Radiation*. Madison, Wisconsin: Sundog Publishing, 2004.
17. Photonics. *The photonics directory 1996-2005*. Photonics.com <http://www.photonics.com/dictionary/lookup/XQ/ASP/url.lookup/entrynum.5323/letter.t/pu./QX/lookup.htm>.
18. Popular Science. *Advanced Tactical Laser: A laser cannon that blasts from the air*. 2005 Popsci.com <http://www.popsci.com/popsci/generaltech/article/0,20967,749736,00.html>.
19. Rozenburg, Vladimir Il'ich *Scattering and attenuation of electromagnetic radiation by atmospheric particles*. [Washington, National Aeronautics and Space Administration] for sale by the National Technical Information Service, Springfield, Va. 1974.
20. Stephens, Graeme L. *Remote Sensing of the Lower Atmosphere*. New York, Oxford, Oxford University Press, 1994 Wikipedia, the free encyclopedia. *Pupil*. 2006 <http://en.wikipedia.org/wiki/Pupil>.
21. Winburn, D.C. *Practical Laser Safety*. New York: Markel Dekker, Inc., 1990.
22. WP_eyecolorsensitivity. *Visible laser light & eye color sensitivity*. Copyright 2004 Power Technology, Inc. http://www.powertechnology.com/PDFs/WP_eyecolorsensitivity.pdf

VITA

Second Lieutenant Scott L. Belton graduated from William J. Bogan High School in Chicago, Illinois. He entered undergraduate studies at Southern Illinois University at Carbondale where he graduate with a Bachelor of Science degree in Electrical Engineering in 2002. Upon graduation, he worked as a teacher in the Chicago Public School System until 2004. He was commissioned through Officer Training School (OTS) May 2004 at Maxwell AFB.

His first assignment was at Wright-Patterson Air Force Base as a developmental Engineer for the National Air and Space Intelligence Center (NASIC). While waiting on his top secret security clearance to process, he completed Air and Space Basic Course (ASBC) in August of 2004 at Maxwell AFB. Immediately following this he was admitted to the Watson Scholars Program allowing him to enroll in the Graduate School of Engineering and Management, Air Force Institute of Technology. Upon graduation, he will be assigned to NASIC as an Advanced Sensors Engineer for three years

REPORT DOCUMENTATION PAGE			Form Approved OMB No. 074-0188		
<p>The public reporting burden for this collection of information is estimated to average 1 hour per response, including the time for reviewing instructions, searching existing data sources, gathering and maintaining the data needed, and completing and reviewing the collection of information. Send comments regarding this burden estimate or any other aspect of the collection of information, including suggestions for reducing this burden to Department of Defense, Washington Headquarters Services, Directorate for Information Operations and Reports (0704-0188), 1215 Jefferson Davis Highway, Suite 1204, Arlington, VA 22202-4302. Respondents should be aware that notwithstanding any other provision of law, no person shall be subject to a penalty for failing to comply with a collection of information if it does not display a currently valid OMB control number. PLEASE DO NOT RETURN YOUR FORM TO THE ABOVE ADDRESS.</p>					
1. REPORT DATE (14March2006)		2. REPORT TYPE Master's Thesis		3. DATES COVERED (From – To) March 2005 – March 2006	
4. TITLE AND SUBTITLE THE SIMULATION OF OFF AXIS LASER PROPAGATION USING HELEEOS			5a. CONTRACT NUMBER		
			5b. GRANT NUMBER		
			5c. PROGRAM ELEMENT NUMBER		
6. AUTHOR(S) Belton, Scott L., Second Lieutenant, USAF			5d. PROJECT NUMBER		
			5e. TASK NUMBER		
			5f. WORK UNIT NUMBER		
7. PERFORMING ORGANIZATION NAMES(S) AND ADDRESS(S) Air Force Institute of Technology Graduate School of Engineering and Management (AFIT/EN) 2950 Hobson Way, Building 640 WPAFB OH 45433-8865			8. PERFORMING ORGANIZATION REPORT NUMBER AFIT/GSS/ENP/06-01		
9. SPONSORING/MONITORING AGENCY NAME(S) AND ADDRESS(ES) N/A			10. SPONSOR/MONITOR'S ACRONYM(S)		
			11. SPONSOR/MONITOR'S REPORT NUMBER(S)		
12. DISTRIBUTION/AVAILABILITY STATEMENT APPROVED FOR PUBLIC RELEASE; DISTRIBUTION UNLIMITED					
13. SUPPLEMENTARY NOTES					
14. ABSTRACT Emerging technology high energy laser (HEL) weapon systems create a myriad of new threats to safety as well as security. One of the primary causes of these concerns is off-axis laser propagation caused by ever-present particulate and molecular scattering medium in the atmosphere. The scatter from these aerosols and molecules can redirect some of the HEL's concentrated energy towards unintended targets such as the eyes of pilots, friendly fighters on the surface, or innocent bystanders. Of particular interest to the laser intelligence (LASINT) community is the possibility that off-axis irradiance from HEL weapon systems could be covertly measured with enough accuracy to provide critical information about HEL weight-power relationships, beam characteristics, and target intelligence information. The purpose of this research is to quantify how much off-axis propagation may occur in specific directions given a set of simulated HEL engagement scenarios involving different HEL characteristics, geometries, and atmospheric conditions. Further simulations assess the amount of information that can be derived about HEL platform characteristics and intended target from remotely measured off-axis intensity via inversion techniques. The High Energy Laser End-to-End Operational Simulation (HELEEOS) software package is used to exploit its fast-running scaling law propagation methods and its robust probabilistic atmospheric database.					
15. SUBJECT TERMS ATMOSPHERIC SCATTERING, MIE SCATTERING, RAYLEIGH SCATTERING, LASER BEAMS, LASER SAFETY, HIGH ENERGY LASERS, LIGHT TRANSMISSION, ELECTROMAGNETIC WAVE PROPAGATION, ABSORPTION, ATMOSPHERIC ABSORPTION, EXTINCTION					
16. SECURITY CLASSIFICATION OF:			17. LIMITATION OF	18. NUMBER OF PAGES	19a. NAME OF RESPONSIBLE PERSON Fiorino, Steven T., Lt Col, USAF (ENP)
a. REPORT	b. ABSTRACT	c. THIS PAGE	ABSTRACT		19b. TELEPHONE NUMBER (Include area code) (937) 255-3535, ext 4506 (Steven.Fiorino@afit.edu)
U	U	U	UU	99	

Standard Form 298 (Rev. 8-98)
Prescribed by ANSI Std. Z39-18